Project information

Project full title	European network for developing new horizons for RIs
Project acronym	EURIZON
Grant agreement no.	871072
Instrument	Research and Innovation Action (RIA)
Duration	01/02/2020 – 31/01/2024
Website	https://www.eurizon-project.eu/

Deliverable information

Deliverable no.	D4.23 (D103)
Deliverable title	Completion of the generic CDR for a fully automated XAS beamline
Deliverable responsible	ESRF
Related Workpackage/Task	WP4 / Task 4.6
Type (*e. g.* Report; other)	Report
Author(s)	M. Nentwich, O. Seeck, M. Krisch
Dissemination level	Public
Document Version	1
Date	31 December 2023 (month 47)
Download page	https://www.eurizon-project.eu/

Document information

Version no.	Date	Author(s)	Comment
1	11 Dec. 2023	M. Nentwich, O. Seeck, M. Krisch	–
2	13 Dec. 2023	M. Nentwich, O. Seeck, M. Krisch	updated Fig. 9 and 10
3	10 Jan. 2024	M. Nentwich, O. Seeck, M. Krisch	Figure axis labels updated; minor text corrections

Contents

Completion of the generic Conceptual Design Report for a fully automated X-ray Absorption Spectroscopy Beamline

1. Abstract

X-ray Absorption Spectroscopy (XAS) is one of the most widespread techniques at synchrotron X-ray facilities with applications across many scientific disciplines with an increased interest by industry, most notably in catalysis, battery research, and material science. This class of experiments requires complex sample environments for *in-situ* and *in operando* studies, a high level of automation, mail-in services, remote access capacities, and automated data analysis.

Here, we present the *Conceptual Design Report* (CDR) for a generic XAS beamline with special focus on full-automatization of *in-situ* catalysis research. The present report will finally consist of three parts: the discussion of the "hardware" design of a generic beamline with one front end in Sec. 4 and of further considerations (*e. g.* automation of alignment, XAS experiments as well as catalysis experiments, (meta-)data storage, use of Artificial Intelligence, required laboratories) in Sec. 5, as well as the model for X-ray tracing calculations.

2. Motivation

Catalysis is one of the key technologies to tackle major challenges within the current energy policy targeting energy sovereignty, reduction of the dependence on fossil and nuclear fuels, and increased utilization of sustainable and renewable fuels. In general, investigating a catalyst implies analyzing the relationships between the structure of a functioning catalyst and its activity under realistic conditions (operando data) [1], see Tab. 1. In addition, the analysis under variable environmental conditions is called *in-situ* and under ambient conditions *ex-situ*. Furthermore, analysis without simultaneous synchrotron or X-ray analysis is referred to as *off-line* in this report [2]. The synthesis of the catalyst material could involve different synthesis routes and starting materials (synthesis data). The structural properties are determined before, during, and after the reaction (characterization data). The reaction itself is characterized by the reaction data and derived quantities (performance data), which serve as input for modeling and simulations, which are the basis for the design of catalytic reactors and processes [1].

Table 1: Categories of catalysis data with some examples.

Synthesis Data	Operando Data	Characterization Data	Performance Data
starting material synthesis routes	temperature pressure flow rate	composition structure	concentration turnover selectivity

The investigation of catalytic processes facilitates efficient conversion processes among all kinds of application areas:

- "energy" (distribution and storage of energy in the form of chemical energy carriers) [3–6],
- "green chemistry" (to close the carbon cycle) [7, 8],
- "earth & environment" (bio-catalysis as part of biotechnology) [9–11], and
- "air & space transportation" (synthetic fuels) [12–14].

Further, electrochemistry plays a key role for the storage of energy, especially for renewable energies. The underlying processes strongly rely on surface chemistry, which requires the same analytic methods as catalysis. Thus, the scientific infrastructure will support both fields. While the overall workflow and basic concepts are similar across those two disciplines, slightly different approaches, different nomenclatures, experimental methods, and property and performance descriptors are used. The necessary and overdue unification is topic of the NFDI4Cat project [1].

The technically most important elements for catalytic experiments are among the transition metals and lanthanides. In order to study the underlying processes and, thus, changes in short and long range order within the (crystal) structure, spectroscopic experiments are perfectly suited. *X-ray Absorption Spectroscopy* (XAS) analyses the energy dependent intensity changes in the vicinity of an absorption edge. The electronic structure of an element under investigation determines, which electronic transitions are possible and, thus, which absorption edges exist. The local environment changes determine significant details of the energy dependent intensity changes, especially for transitions concerning the inner most shells (K and L edges). Exactly those edges of the technically interesting elements are located in the energy range of 5 keV to 40 keV, see Fig. 1.

The complete experimental process, from aligning the beamline via XAS or catalysis experiments to the combined *in-situ* XAS experiments can strongly benefit from automatization. Both in academia and specifically in industry, the largest costs are personnel. Thus, reducing their work load by automatizing repetitive work will strongly increase effectivity. Additionally, the reproducibility of the measurements will strongly increase, which is also a huge gain for industrial and academic questions.

While already different approaches exist to simplify and automatize XAS experiments, often the basic alignment task are still neglected at many beamlines. Whatsmore, catalytic experiments – typically having an enormous parameter space – are hardly automatized. An increase in the degree of automatization would mean a reduced effort for exploring the parameter space in a brute force manner. Further, the automatization would be accompanied with the standardization of the data management to facilitate the FAIR principles (findability, accessibility, interoperability, and reuse of digital assets) [16]. The consortium NFDI4Cat is working on realizing those principles within the German catalyst community [1]. The principles feature the machine-accessibility, which, on the one hand, facilitates the structured analysis of own data, and on the other hand the possibility to compare with data of other scientists.

Based on highly standardized data and well-organized meta-data, machine learning and artificial intelligence could reduce the reasonable parameter space while measuring. In turn, this will enhance the data quality and the sample throughput.

In general, these improvements will increase the attractiveness to industry and non-expert users and, thus, speed-up the innovative process within Germany. Further, an increase of remote and mail-in experiments will be facilitated.
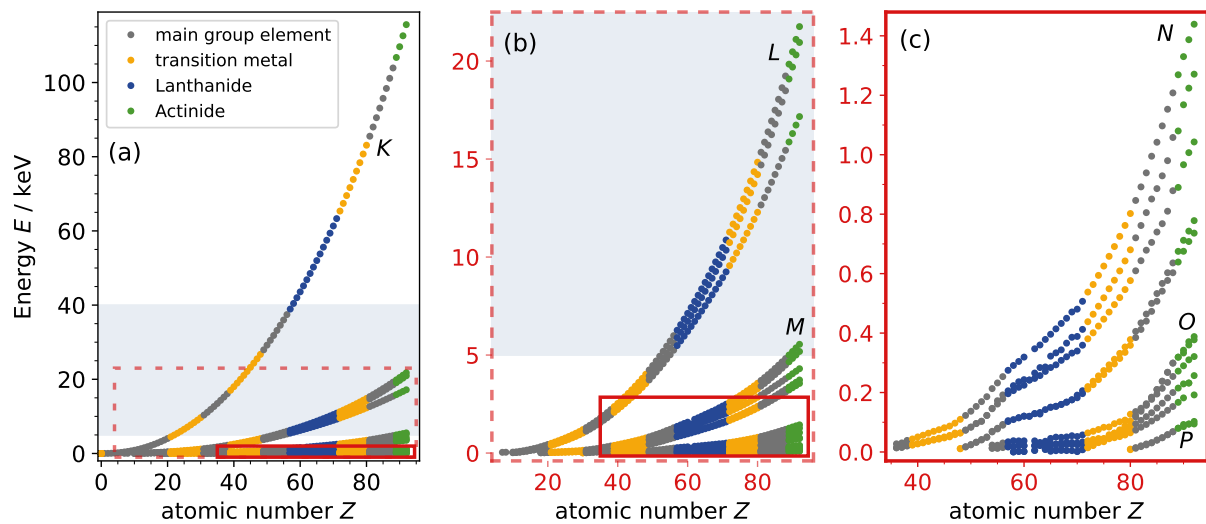
Figure 1: Energies of different absorption edges in dependence of the elements up to atomic number 92, according to X-ray Data Booklet [15]. The gray area highlights the energy range covered by a typical hard X-ray spectroscopy beamline.

3. Preparations

In preparation of the CDR, plenty of information covering the divers topics of a fully-automated *in-situ* XAS beamline had to be collected. A list of those topics is given in Tab. 2, along with projects dedicated to them.

Table 2: List of those topics related to a fully-automated *in-situ* XAS beamline, along with projects dedicated to them.

Topic	Project
State-of-the-Art XAS beamlines	
Requirements of catalysis experiments	NFDI4CAT
Challenges and aspects of automatization of a beamline	ROCK-IT [17]
Integration of sample environments into beamline control	SECoP [18], NICOS [19]
Demands of (meta-)data storage	DAPHNE4NFDI [20]
Advantages and perspectives of Artificial Intelligence	

Information to these topics were assembled by joining different kinds of meetings related to the listed projects and also by dedicated research also including the basic knowledge gained by these meetings.

3.1. Attended Meetings, Workshops, and Beamtimes

By attending meetings and workshops of the projects mentioned in Tab. 2, not only an elemental knowledge about the relevant topics was build-up, but also a network of experts was established, who could answer more detailed questions. A list of attended meetings, which were highly valuable for D4.23 is listed in Tab. 3.

Table 3: List of attended meetings and workshops, which were highly valuable for D4.23.

Name	Date	Place	further reading
DAPHNE4NDFI work meeting	5 – 7 December 2022	Hamburg	[21]
DESY Users' Meeting	23 – 27 January 2023	Hamburg	[22]
Hands on Workshop for SECoP	22 – 23 February 2023	Berlin	[23]
ROCK-IT project meeting	13 – 14 September 2023	Karlsruhe	

Additionally, in order to understand the practical details of *in-situ* XAS experiments, several beamtimes with related scope were attended. Table 4 gives on overview of those beamtimes.

Table 4: List of attended beamtimes, which were highly valuable for D4.23.

PI	Date	Beamline
Jan-Dierk Grunwaldt	9 – 13 March 2023	P64
Dmitry Doronkin	23 – 28 March 2023	P65
Anna Zimina	7 – 11 December 2023	P65

3.2. Survey of existing and planned spectroscopy beamlines

An additional preparation for the CDR was a comprehensive survey of existing and planned spectroscopy beamlines at 4th Generation Synchrotron Rings (4GSR). This extensive overview allows to determine the most important elements of a spectroscopy beamline and reasonable distances from the source.

Currently, many synchrotrons worldwide are on the way to becoming 4th generation or have even finalized this step. Figure 2 gives an overview of those synchrotrons and their current stages. Because of the high and further growing importance of spectroscopic analysis, all of the 4GSR will have dedicated spectroscopy beamlines.

Running
- ESRF-EBS (France)
- MAX IV (Sweden)
- Sirius (Brasil)

Under Construction
- APS-U (USA)
- SPring8-II (Japan)
- HEPS (China)

In Planning
- PETRA IV (Germany)
- ELETTRA II (Italy)
- SLS-II (Switzerland)
- Pohang Light Source (Korea)

Considering an Upgrade
- SKIF (Russia)
- ALS-U (USA)
- Soleil (France)
- Diamond (UK)

Figure 2: Overview of the different stages of becoming a 4th Generation Synchrotron and the corresponding synchrotrons.

In order to gain an overview of the most important components of hard X-ray spectroscopy beamlines, we studied those beamlines with available design details of the 4GSR,
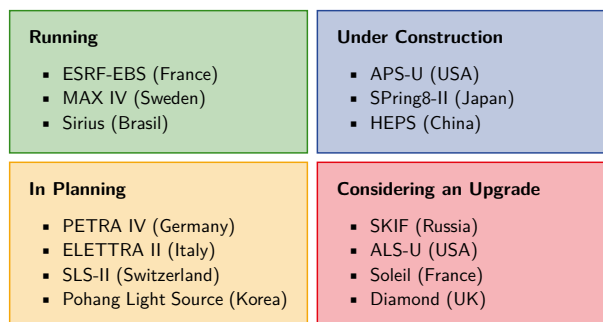
which are currently running or under construction. We summarized the results in Tab. 5. Additionally, we created a list with the distances of the most important optical elements, see Tab. 7.

The overall design consists of one or several, complementing undulators, typically covering an energy range of 4 keV to 30 keV. Further, a monochromator with high energy resolution is strongly desired. The focusing is generally performed by focusing mirrors (toroid or Kirkpatrick Baez mirrors) and only rarely by transfocators. The mirrors sometimes also serve as *White Beam* (WBM) or *Harmonic Rejection Mirrors* (HRM). Additionally, attenuators are sometimes installed to reduce the intensity on highly sensitive samples. In order to offer more versatile scopes, most beamlines possess several end stations with different, highly specialized equipment. The total length of the beamline is predominantly defined by the synchrotron ring circumference (defining the position of the first optical element, see Sec. 4) and the scope of the beamline (strong focus or high beam stability).

Table 5: Beamline parameters of existing spectroscopy beamlines of 4GSR. (WBM – White Beam Mirror, KB – Kirkpatrick-Baez mirrors, DCM – Double Crystal Monochromator, H – horinzontal(ly), D – detector, A – analyzer, S – spectrometer), HRM – Harmonic Rejection Mirrors

parameter	unit	Polar 4-ID, APS-U [24]	XPCS 8-ID, APS-U [24]	Balder, MAX IV [25, 26]	ID24 EDXAS_L, EBS-ESRF [27]	ID26, EBS-ESRF [28, 29]
Ring						
electron beam energy	GeV	6	6	3	6.037	6.037
electron beam current	A	0.2	0.2	0.25	0.2	0.2
Undulator						
undulator type		2 in-line SCAPE[a]	2 in-line revolver	in-vacuum, tapered	4 in-line, 'tapered'	3 in-line
undulator length	m	2 × 1.3	4.6	2.0	≈ 3 × 1.5	3 × 1.6
period	mm	35 + 35	21/25	50	27 + 27 + 27/32 + 32	35 + 35 + 35
k value		N/A	1.29/1.90	9	N/A	2.45
minimal gap	mm	N/A	N/A	5.5	e.g. 11.0/11.7/12.5	11.2
energy range	keV	2.8 to 27	8 to 25	2.4 to 40	5 to 28	2 to 25
Monochromator						
optical elements		WBM (Si, Pt, Rh)	WBM (Si, Cr, Pt, Rh)	WBM (Si, Ir)	KB-V = WBM (Si, Pt, Rh)	WBM (Si, Pt, Pd)
monochromator		H DCM, Si(111), LN$_2$ cooled	H DCM, Si(111) and Si(311), LN$_2$ cooled	DCM, Si(111) and Si(311), LN$_2$ cooled	polychromator, Si(111), Laue geometry	DCM, Si(111) and Si(311), LN$_2$ cooled
offset	mm	N/A	15	10 to 32	N/A	25
End Station						
no. end stations		2	2	1	2	2
dist. source to sample	m	61.3/73.3	56.3/67.5	46.0	55.6/64.7	43.0/54.6
focusing elements		transfocators, KB mirrors, toroidal mirrors	transfocators, KB mirrors	toroidal mirror	KB mirrors	bendable KB mirrors
beam size	μm^2	34 × 4	0.3 × 0.3	100 × 100	4 × 4	100 × 50
flux	ph/s	N/A	N/A	1 × 10$^{13\,b}$	4 × 10$^{13\,c}$	5 × 10$^{13\,d}$
diffractometer		double tilt Eulerian cradle	double tilt Eulerian cradle	1 axis	breadboard	breadboard
detectors etc.		2D fluorescence D, polarization A, Raman S	N/A	Raman S, mass S, X-ray emission S, Lytle D, PIPS D, SDD	2D FReLoN CCD, 1D Hamamatsu CCD, XH Ge microstrip	photo diodes, hard X-ray emission S tender X-ray emission S, SDD

a – SuperConducting Arbitrarily Polarizing Emitter,   *b* – over complete energy range,   *c* – 24 keV,   *d* – no details given

Table 6: Beamline parameters of existing spectroscopy beamlines of 4GSR. (WBM – White Beam Mirror, KB – Kirkpatrick-Baez mirrors, DCM – Double Crystal Monochromator, H – horinzontal(ly), D – detector, A – analyzer, S – spectrometer), HRM – Harmonic Rejection Mirrors

parameter	unit	EMA, Sirius [30, 31]	QUATI, Sirius [32]	P62, PETRA III [33]	P64, PETRA III [34, 35]	P65, PETRA III [36]
Ring						
electron beam energy	GeV	3	3	6	6	6
electron beam current	A	0.1	0.1	0.1	0.1	0.1
Undulator						
undulator type		in-vacuum	dipole source	undulator	undulator	mini-undulator
undulator length	m	1.2	N/A	2	2	0.39
period	mm	20	N/A	31.4	32.8	32.8
k value		N/A	N/A	2	2.6	2.6
minimal gap	mm	22	N/A	N/A	10	10
energy range	keV	2.7 to 30	4.5 to 35	3.5 to 35	4 to 44	4 to 44
Monochromator						
optical elements		HRM (Si, Pt, Rh)	WBM (Si, Pt, Rh)	HRM/WBM (B$_4$C, Pt, Rh)	WBM (Si, Pt, Rh)	WBM (Si, Pt, Rh)
monochromator		DCM, Si(111) and Si(220), V bounce, fixed exit	DCM, Si(111) and Si(311), LN$_2$ cooled	DCM, Si(111) and Si(311), LN$_2$ cooled	CCM and DCM, Si(111), Si(311), LN$_2$ cooled	DCM, Si(111) and Si(311), H$_2$O cooled
offset	mm	0	N/A	14	21	N/A
End Station						
no. end stations		2	2	1	1	1
dist. source/sample	m	45.5/98	45.5		87.2	N/A
focusing elements		KB mirrors	toroidal mirror (Pt, Rh)	CRL (2D Be)	mirrors (Si, Rh)	–
beam size	μm^2	1 × 0.4	10 × 5	100 × 4 to 2000 × 1000	150 × 50	500 × 1000
flux	ph/s	1 × 10^{12e}	1 × 10^{10e}	1 × 10^{13f}	1 × 10^{13f}	2 × 10^{12f}
sample stage		6+2 circles	breadboard	breadboard	breadboard	breadboard
detectors etc.		2D, Raman-S, photodiodes, ion chamber, fluo D	Raman-S	2D,	fluorescence D, transmission D, ion chamber, dispersive von-Hamos S	ion chamber, HPGe D, Si-PIPS^g diodes, fluo D

e – 20 keV,   *f* – 9 keV,   *g* – Passivated Implanted Planar Silicon

Table 7: Overview of the distances of beam shaping elements at different spectroscopy beamlines of 4GSR. If distances for several focusing variants are given, only one of them is active in each individual experiment.

	Polar 4-ID B [24]	XPCS 8-ID E [24]	Balder[a] [25, 26]	ID24 EDXAS_L [27]	ID26, EH1 [28, 29]
aperture	27.0	27.1	-	N/A	-
WBM/HRM	2 × 28.5	28.0 + 30.6	26.5 + 31.5	28.5 + 31.0	29.7
monochromator	30.0	33.7	28.0	55.0[b]	33.4
aperture	31.1	-	31.0	N/A	34.2
aperture	47.3	51.3	-	N/A	-
Focusing toroid mirrors	48.0 + 50.0	-	31.5	55.5	-
KB mirrors	61.0	55.3	-	28.5 + 31.0	37.2 + 39.1
transfocators/CRLs	59.3	52.0	-	-	-
attenuators	54.1	N/A	N/A	N/A	41.9
aperture	53.7	54.8	32.0	N/A	42.0
aperture	59.4	55.9	-	N/A	-
sample	61.3	56.3	46.0	55.6	43.0

	EMA [30, 31]	QUATI [32]	P62 [33]	P64 [34, 35]	P65 [36]
aperture	N/A	N/A	47	44.8 + 37.1	49.0
WBM/HRM	2 × 33.3[c]	15.0 + 30.0	54.5 + 56.5	58.7 + 60.1	50.0 + 53.0
monochromator	28.5	24	52	56.6	51.5
aperture	N/A	N/A	57	-	-
aperture	N/A	N/A	-	-	-
Focusing toroid mirrors	-	30	-	-	-
KB mirrors	44.5 + 96.0	-	-	-	-
transfocators/CRLs	-	-	59 + 70	-	-
attenuators	45, 97	N/A	-	N/A	N/A
aperture	-	N/A	60	87	59
aperture	-	-	71.5	-	N/A
sample	98	45	72 to 77	87.2	60

a – values are rough estimates based on Fig. 1 of [25]
b – polychromator used after KB mirrors
c – Harmonic Rejection Mirrors, after monochromator

4. Physical Design of the Beamline

The physical design of a beamline depends on multiple factor, *e. g.* methods, material, type of experiment, desired resolution in time and space, ring parameters like circumference and available energy. While some of those aspects are already clearly defined, some others are still open. In order to develop the greatest possible synergy with other projects, the X-ray tracing (xrt) models will be based on the upcoming PETRA IV *Applied Analytical and Q-EXAFS* beamline (AppAnaXAFS; current beamline P65 of PETRA III). The future of the beamlines is already topic of the PETRA IV upgrade [37] as well as of the ROCK-IT project [17]. In addition to the design relevant for this beamline, we will also discuss general options and decision making.

The beamline and its elements were simulated with the python module for X-ray tracing "xrt" [38]. The models especially served to determine reasonable properties for different optical elements (including positions, coatings, and lengths). The interested reader is free to adapt the model for individual tests using the provided files [39].

4.1. Scientific Scope

The scientific scope of a beamline determines its most important properties, like spatial and temporal resolution, energy range, and available space for sample environment cells. For the present case of the Applied Analytical and Q-EXAFS beamline [40], the spectroscopic measurements require a large energy range, covering the K and L edges of the most interesting elements of the catalytic experiments (transition metals as well as lanthanides and actinides). Thus, the energy range of 4 keV to 40 keV is desired, see also Fig. 1. Additionally, the fast spectroscopic scans, so called *Quick EXAFS* (Q-EXAFS) scans, will be realized by a Q-EXAFS monochromator, see Sec. 4.5, combined with a broad, continuous spectrum.

The continuous spectrum required by the Q-EXAFS monochromator can be realized by a Wiggler or Bending Magnet, see Sec. 4.4. For the AppAnaXAFS beamline, the application of a 3-pole Wiggler is desired. The time resolution of the XAS experiment is mainly defined by the speed of the catalytic reaction, which is usually in the range of sub-seconds. The beam size should be in the range of the sample size, which is often a capillary of few mm size. The equipment of the sample environment can be fairly extensive, including gas mixing systems, heating/cooling setups, and battery testers, see Sec.4.9.1. Additionally, the design of the sample environment cells must be suitable to the intended experiment, *e. g.* enabling the transmission of the beam through the cell, which is a material-dependent process, defining a minimum energy. The beamline is also dedicated for high throughput application, which requires high stability not only of the beam position, but also of the whole setup including undulator and monochromator.

4.2. Storage Ring Parameters

The planning of the upcoming PETRA IV storage ring is in a very intense state, preliminary values of the ring are already available [41], see Tab. 8. The AppAnaXAFS beamline will be located in the new west hall of PETRA IV, where the distance between ID and tunnel wall are 40 m [42].

Table 8: Storage ring parameters of the present calculations for PETRA IV [41].

parameter	unit	brightness mode	timing mode
electron beam energy	GeV	6.0	
β	m^2	2.2×2.2	
emittance	pm rad^2	20×4	
circumference	m	2300	
tunnel width	m	3.1	
energy spread	1×10^{-3}	0.9	1.2
electron beam current	mA	200	80

4.3. General Layout

The upcoming sections will include discussions about different options for components of the AppAnaXAFS beamline. The main task is the evaluation of the suitability of a 3-pole Wiggler for future applications. In general, this Wiggler should enable the fast Q-EXAFS scans while providing a flux of 10^{12} photons on the sample. If the flux is too low, the wiggler must be dispensed with in favor of an undulator, which means that Q-EXAFS scans become considerably more complicated and suggest the use of a tapered undulator.

The main components of the AppAnaXAFS beamline are listed in Tab. 9 together with their respective positions along the beam, as well as a remark to a more detailed discussion in upcoming sections. These elements will be used for the upcoming xrt calculations.

Table 9: Beamline components and their distances from the source (center point). Two alternative positions for the mirrors are discussed in detail and listed in the table.

component	description	section	distance from source / m
insertion device	3-pole Wiggler	Sec. 4.4	0.0
apertures	photon shutter PS1		19.0
	photon shutter PS2	Sec. 4.4	35.0
	main beam shutter shutter		37.0
mirrors	collimating	Sec. 4.6	21.0 and 42.0
	plane, redirecting	Sec. 4.6	23.0 and 44.0
monochromator	Quick-DCM Si111 and Si311,	Sec. 4.5	47.0
	DCM Si111 and Si311		48.0
sample position	mechanical positioning system	Sec. 4.9.1	55.0
	sample environment equipment	Sec. 4.9.3	

4.4. Insertion Device

In order to turn the electron beam in synchrotron radiation, a suitable insertion device (ID) is needed. For spectroscopy beamlines, the continuity of the energy generally has a higher priority compared to the flux. The optical properties of an insertion device are characterized by the K value

$$K = 0.934 \cdot \lambda_u[\text{cm}] \cdot B_0[\text{T}],\qquad(1)$$

with the period of oscillations λ_u and the amplitude of the magnetic field B_0 [43]. A device with high K value ($K \gg 1$) has a stronger influence from higher harmonics as well as lower intensity, lower collimation, higher emittance, and smaller coherence, see Tab. 10. Insertion devices with high K values are favored for spectroscopy beamlines and are called Wiggler; low K value devices are called undulators.

Table 10: Comparison of different properties of Wiggler and Undulator with N periods [43].

property	wiggler	undulator
angle of transverse oscillation	large	small
interference	no	yes
K value	$\gg 1$	≈ 1
# harmonics	high	low
radiated energy	broad continuum	narrow at well defined E
intensity increase	$2N$	N^2
degree of collimation	low	high
emittance	high	very low
integral photon flux	same	same
coherence	no	yes
section	low β	high β

Depending on the parameters of the ID, the bandwidth of the generated X-ray beam differs significantly. Setting the X-ray energy of the experiment when using a wiggler is solely determined by the Bragg angle of the monochromator (see Sec. 4.5) as the photon flux of the source hardly depends on the X-ray energy. In contrast, for undulators, the flux is strongly dependent on the X-ray energy and the chosen undulator gap, which determines the magnetic field within the undulator.

To enable high temporal resolution, as is often required for catalytic experiments, special considerations must be made for the setup and data handling. These scans are referred to as Quick EXAFS (Q-EXAFS) scans and typically cover a 1 s-scan of 1000 steps within an energy range of 1000 eVfor EXAFS regime and a 100 ms-scan of 1000 steps within an energy range of 100 eVfor XANES regime [44]. An important basis for these scans is a nearly constant primary beam

with respect to total flux, but also to intensity distribution within the beam and beam position. Generally, two main approaches exist: (1) an ID with a broad and nearly uniform beam is used, where only the monochromator setting determines the beam energy or (2) an ID with a narrow energy bandwidth is used, where both ID and monochromator must move to determine the beam energy. The latter case describes the use of an undulator as ID and the movement of its gap to adjust the energy. However, this motor is slow and limits the time resolution to minutes and seconds. In this variant, monochromator and undulator are moved in continuous scans as currently done at P64 and P65 of PETRA III [45]. In contrast, version (1) is faster, especially when combined with a Q-EXAFS monochromator (see Sec. 4.5). The required broad energy bandwidth can be provided by using a tapered undulator [46–48]. Further, Wigglers naturally offer a nearly continuous spectrum, especially for very low period numbers, at the cost of high divergence.

For the AppAnaXAFS beamline, the use of a 3-pole Wiggler is desired [49–51], having highly similar characteristics to Bending Magnets, but providing compatibility with a 4GSR source. However, 3-pole Wiggler also have a high beam divergence and thus large beam sizes. First considerations of a 3-pole Wiggler setting resulted in beam sizes of roughly $28 \times 3 \, \mathrm{mm}^2$ at the position of Photon Shutter PS1 (see Tab. 11 for more details on the safety shutters within the tunnel), see also App. A. The vertical extension of the beam will exceed the acceptance of PS1, see Fig. 3. Possible solutions to this issue will be discussed in the upcoming sections 4.6 and 4.7.

Table 12 contains a list of the Wiggler parameters used for the xrt calculations (see App. A) of the AppAnaXAFS beamline. As the 3-pole Wiggler is a very special insertion device, the PETRA IV project team recommended to use the class `SourceFromField` instead of the convenient `Undulator` or `Wiggler` class, employing a `customField` data file of the magnetic field, cf. Fig. 4 [52].

Table 11: Location and size of the mandatory safety shutters within the tunnel.

shutter name	dist. from source / m	opening / mm^2
Photon Shutter PS1	21	12×6
Photon Shutter PS2	35	10×6
Main Beam Shutter MBS	37	20×10

Table 12: Key parameters of the 3-pole Wigglers at the AppAnaXAFS beamline [52, 53].

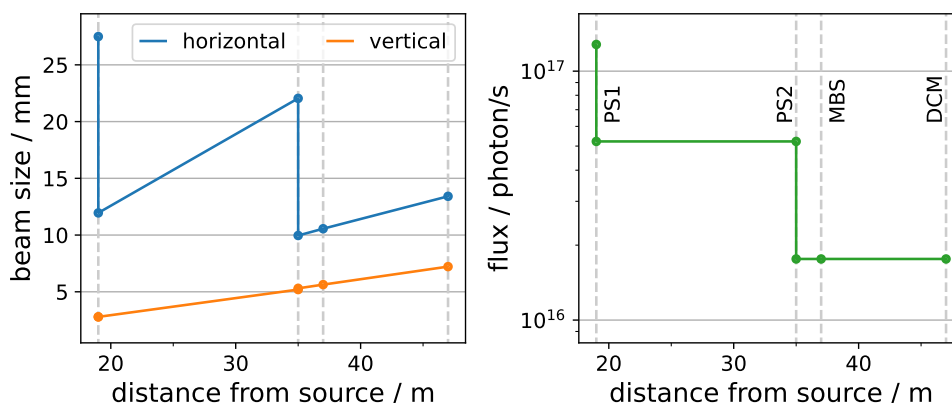| parameter	unit	TP2
length	m	0.142
period length	cm	14.2
# of periods		1
K value		11.5
E range	keV	4 to 40
max. magn. field	T	0.863
total power	kW	0.347

Figure 3: Beam size (FWHM) and flux calculated with xrt for the non-collimated beam at different positions along the AppAnaXAFS beamline. The influence of the photon shutters PS1 and PS2, the main beam shutter (MBS) as well as the monochromator are considered.

4.5. Monochromator

The polychromatic X-ray beam provided by the ID needs to be monochromatized for most experiments. By reflecting the beam at a perfect single crystal, only one wavelength (and its harmonics) is selected, with the bandwidth corresponding to the Darwin width of the reflecting crystal [54]. In order to keep the exiting beam parallel to the incident beam double bounce monochromators have become established.
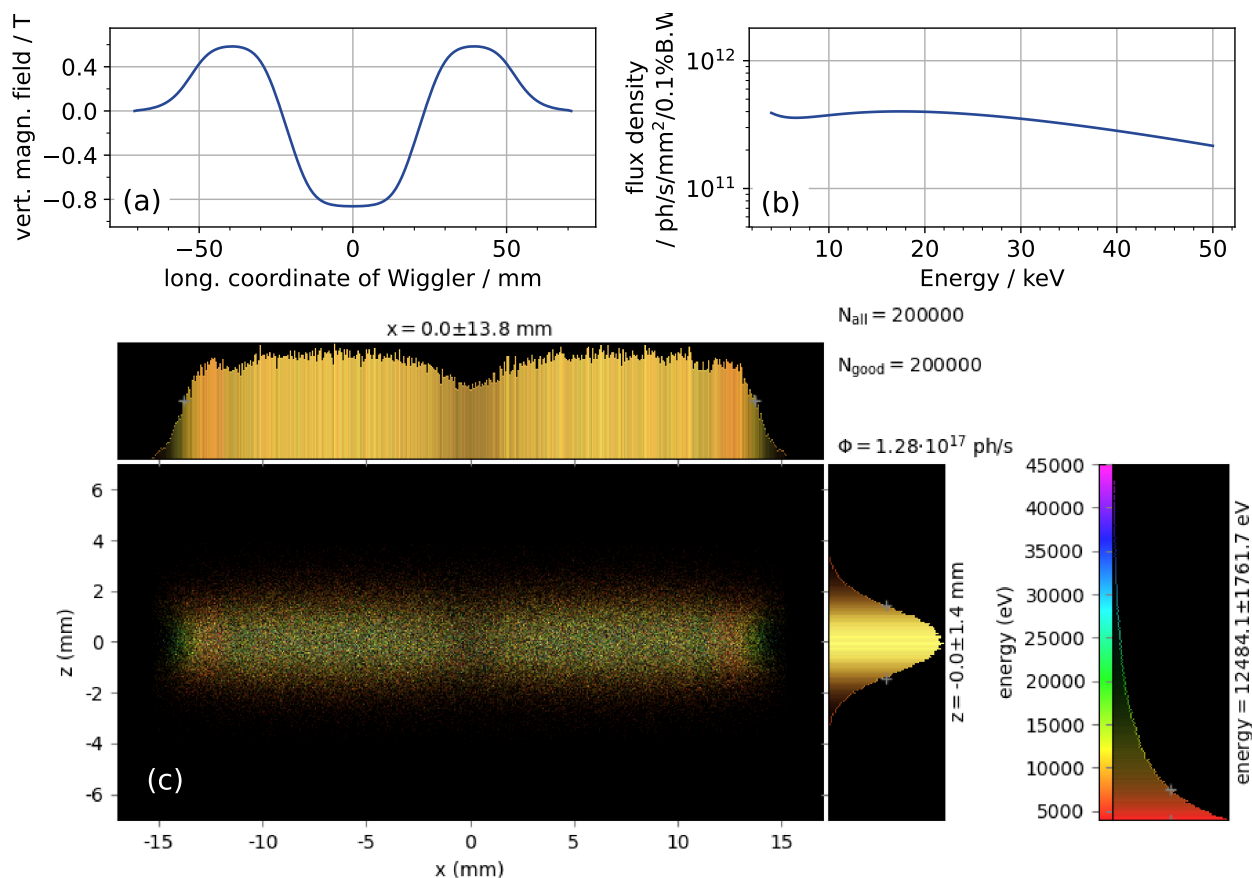
Figure 4: (a) Vertical magnetic field, (b) flux density, and (c) beam profile of the 3-pole wiggler as provided by the PETRA IV working group [52].

The standard monochromator of the analyzed spectroscopy beamlines in Sec. 3 is a Si(111) double crystal monochromator (DCM), which is best suited for the energy range of $2\,\mathrm{keV}$ to $20\,\mathrm{keV}$ and even above. This DCM is is often complemented by a Si(311) DCM for energies above $10\,\mathrm{keV}$ [55].

Further, the majority of the monochromators are cooled, mainly with liquid nitrogen. The high flux at 4GSR in combination with the generally high power of undulators requires extra cooling of the monochromator, independent of the choice whether to use White Beam Mirrors (WBM, see Sec. 4.6) to reduce the heat load. However, the power of the 3-pole Wiggler relatively low with $0.347\,\mathrm{kW}$, so that water cooling might be sufficient.

Especially for spectroscopic experiments, where the Bragg angle of the monochromator is permanently changing, a perfect alignment of both crystals with respect to each other is crucial. In order to improve the overall beam stability (at cost of flexibility), the reduction of vibrations from the second DCM crystal could be decreased by using a *Channel-Cut Crystal Monochromator* (CCM). These monochromators are produced by cutting a channel into a single crystal and, thus, have a compact and cost effective design while reducing vibrations and alignment complexity [54, 56]. In order to guarantee for exactly the same lattice parameters of both crystals, especially their temperature has to be identical. Thus, direct, thermal coupling is highly important. Additionally, the heat load on the first crystal would naturally be much higher when the white beam directly hits the monochromator, thus WBMs are mandatory.

Although the exit beam of a CCM is parallel to the incident beam, its height changes slightly when the energy is varied, resulting in different parts of the sample being examined as the energy is scanned, unless the sample height is corrected.

In order to avoid that effect, the use of two successive, identical CCM would cancel out the beam offset and create energy independent conditions (Bartels's type or four-bounce monochromator) [57–59]. Naturally, this setup corresponds to multiple diffraction of the beam, such that the reflected beam is of higher index, which leads to a sharpened beam and higher energy resolution with almost no additional loss of intensity [57, 60]. Calculations with xrt revealed an additional intensity loss due to the second monochromator of $1.6\,\%$ over the complete energy range. Figure 5 shows the development of the relative flux over the desired energy range. Unfortunately, the synchronization of both CCMs is now the biggest challenge.

In order to ensure Q-EXAFS scans, a very fast and reliable change of the X-ray beam energy is necessary. The best time resolution can be achieved by using especially designed Q-EXAFS monochromators, which facilitate fast energy scans in a limited energy range of ≈ 1 keV.

Generally, moving the undulator gap is much slower (see also Sec. 4.4) than changing the Bragg angle of the monochromator, which is why the undulators are often kept at a certain base energy and the monochromator scans through the available bandwidth. When using an undulator as source, an artificial broadening of the bandwidth can be realized by tapering, see Sec. 4.4. Different approaches of Q-EXAFS monochromators are discussed in literature [61–63]. Additionally, a fast and synchronized readout of the intensity and energy data is crucial, which is best realized by the use of ionization chambers and ADCs, see Sec. 4.9.2.
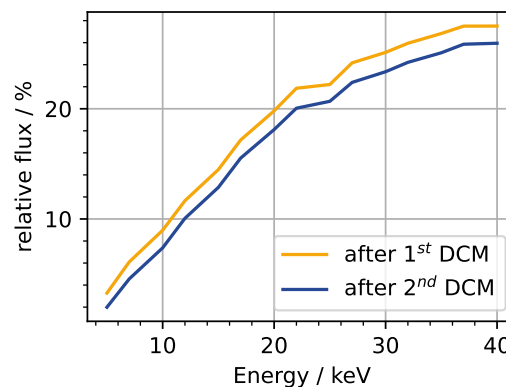
Figure 5: Normalized flux of the X-ray beam after the 1st and 2nd CCM with respect to the flux before the 1st CCM (discontinuities caused by changing the undulator harmonics).

4.6. Harmonic Rejection Mirrors and White Beam Mirror

Several mirrors can be placed along a beamline serving different purposes, *e. g.* for collimation/focusing (see Sec. 4.7), rejection of harmonics, and to protect the monochromator against excessive heat load [64]. All or parts of the functions can also be combined in the same mirror.

4.6.1. Harmonic Rejection Mirrors

Harmonic Rejection Mirrors (HRM) can be placed before and after the monochromator and serve to suppress unwanted harmonics that could cause drastic errors in the absorption coefficient and thus falsify the results [65]. In order to create this effect, the specular reflectivity of the mirror material is used, which has a sharp cutoff at a characteristic photon energy, see Fig. 6. Thus, these mirrors work as low-pass filter [65] and typically have stripes of different coating materials (*e. g.* B_4C, Pd, Rh) in order to vary between different base energies for the experiment. Please note that low incidence angles always mean a large footprint and thus necessitate long mirrors, which are more challenging to produce with high quality at higher costs.

4.6.2. White Beam Mirrors

Generally, *White Beam Mirrors* (WBM) are installed as first optical element of the beamline in order to reduce the enormous heat load of the upcoming, more delicate elements. This reduction occurs by absorption of photons with energies above the critical energy of the surface material (also depending on the angle of incidence, see Fig. 6) [66].

Heat load is not only a problem in itself, but the resulting temperature gradient must also be reduced to decrease internal stress that otherwise leads to deformation and surface deterioration. For mirrors, the reduction of heat load and thermal gradient must be managed by passive and active cooling [66]. Other approaches (*e. g.* for monochromators as first optical element) are filters based on reflection or on absorption as well as pre-monochromators.

In the present case of the AppAnaXAFS beamline, the DESY philosophy must be taken into account, according to which a small crystal (monochromator) is preferably cooled instead of a large mirror. The argument behind this philosophy is that thermal distortions of the large mirror surface significantly influence the beam properties, while the monochromator is less sensitive to surface defects. For the planned 3-pole Wiggler no special requirements are needed to safely handle the heat load at the first optical element (presumably a collimating mirror), as the total power of the Wiggler is only 0.347 kW.

4.6.3. Collimating/Focusing Mirrors

One of the most important applications of an X-ray mirror is beam focusing (and collimation). In general, the mirrors are distinguished whether they influence only one or both dimensions of the beam (hereinafter referred to as 1D and 2D). The simplest shape, and thus the cheapest manufacturing option, is the bendable flat mirror. The 2D alternative corresponding to this 1D mirror is the toroidal mirror, which is in principle a curved or bendable, longitudinal section of a cylinder. Additionally, we will also study the effect of 1D and 2D parabolic mirrors on the beam shape.

For the "spherical" mirrors (toroidal and bent flat), the radii for meridional and sagittal focusing are given by the Coddington equations

$$R_m = \frac{2pq}{p+q} \cdot \frac{1}{\sin\theta}, \qquad\qquad R_s = \frac{2pq}{p+q} \cdot \sin\theta, \qquad (2)$$
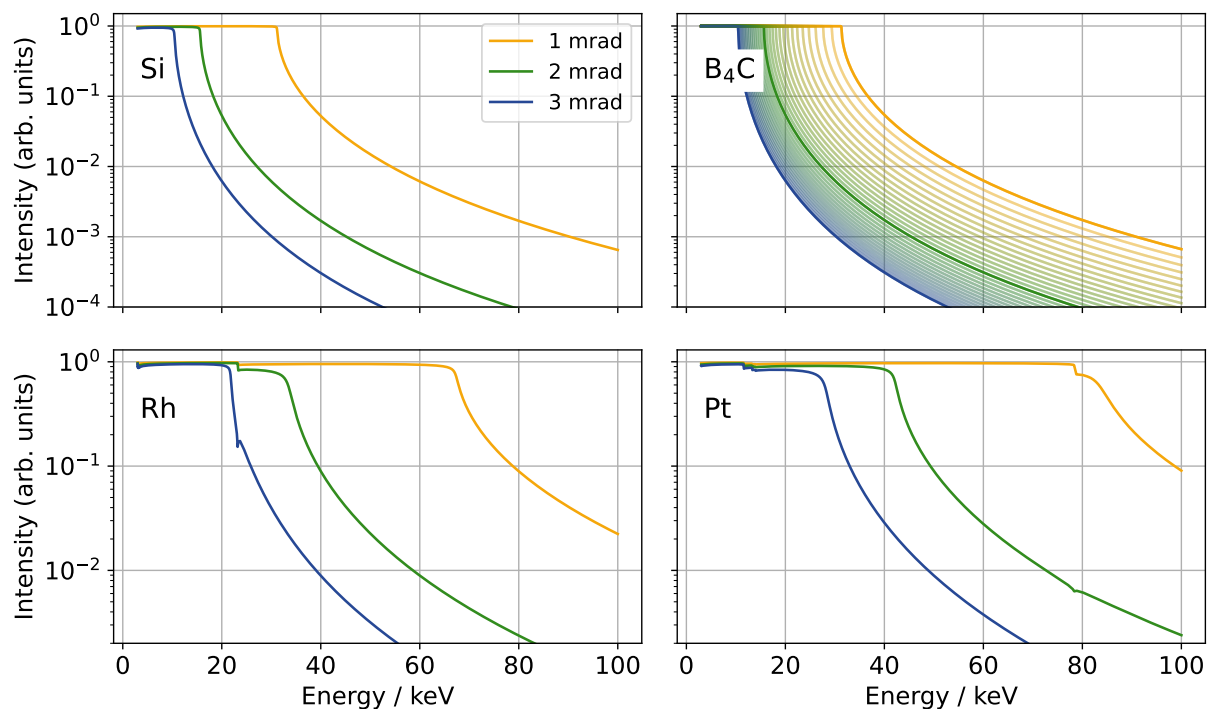
Figure 6: Reflectivity curves of different coating materials and different incidence angles.

with the incidence angle θ as well as the object distance p and the image distance q, respectively [38, 66]. Parabolic mirrors only consider two cases: the beam is divergent and should be collimated or the beam is parallel and should be focused. In case of collimating mirrors, the image distance is set to infinity [67]. Parabolic mirrors have a better collimation performance in comparison with spherical mirrors [68].

The most prominent example of focusing mirrors are the Kirkpatrick Baez mirrors [69]: a pair of mirrors consisting of a horizontal and vertical focusing unit, respectively.

Of course, alternative focusing methods exist, of which the mirror is the most suitable approach with respect to spectroscopic applications. Section 4.7 describes the alternatives along with their advantages and disadvantages.

4.6.4. Considerations for AppAnaXAFS

At PETRA IV the intended 3-pole wiggler of the AppAnaXAFS beamline will have a highly divergent beam, implying large beam sizes. However, the footprint on the monochromator must have a reasonable size and Bragg's Law must remain applicable. Thus, a (vertical) beam collimation is strongly intended, which reduces the (vertical) beam divergence (and size) while preserving the flux. However, the beam should not be affected in horizontal direction, as this generally worsens the energy resolution by changing the direction of the beams and affecting the incidence angle. This collimating mirror should be located as close to the ID as possible.

By default, mirrors are placed outside the ring tunnel to allow access to the mirror (for repair and maintenance) even when the synchrotron is in operation. However, first xrt calculations including photon shutters and main beam shutter (opening of $10 \times 6 \, \text{mm}^2$ and $20 \times 10 \, \text{mm}^2$, respectively [42]) revealed a beam size of $27 \times 14 \, \text{mm}$ behind the wall at $\approx 47 \, \text{m}$ (see Fig. 3). A collimation beyond this point would merely preserve this beam size. Additionally, the flux is already reduced by a factor 2 to $1.74 \times 10^{16} \, \text{photon s}^{-1}$ due to apertures realized by the safety shutters. As enlarging the maximum shutter openings is a challenge from a technical and safety point of view [42], the aim is to position the collimating mirror closer to the source. A solution of this conflict could be the application of a collimating mirror before exiting the tunnel. Together with the Beamline Technology Department, the necessary equipment within the tunnel for a default beamline was discussed, including their positions [42]. Furthermore, the fact was highlighted that the utilization of a solitary mirror would inevitably alter the direction of the beam, which would significantly increase the complexity of the design of the beamline itself and the adjacent beamlines. In order to keep the design more simple and flexible, the use of mirror pairs was strongly recommended. As a result, Fig. 7 was developed, highlighting three possible positions for the placement of the collimating mirror and its redirecting counterpart: **O**utside the tunnel, close to the **W**all (OW); **I**nside the tunnel, close to the **W**all (IW); **I**nside the tunnel, close to the **I**D (II). Beam decoupling, fast shutter, dump magnet, photon shutter PS1, vacuum components, and diagnostic units require the

This project has received funding from the European Union's Horizon 2020 research and innovation programme under grant agreement No. 871072.
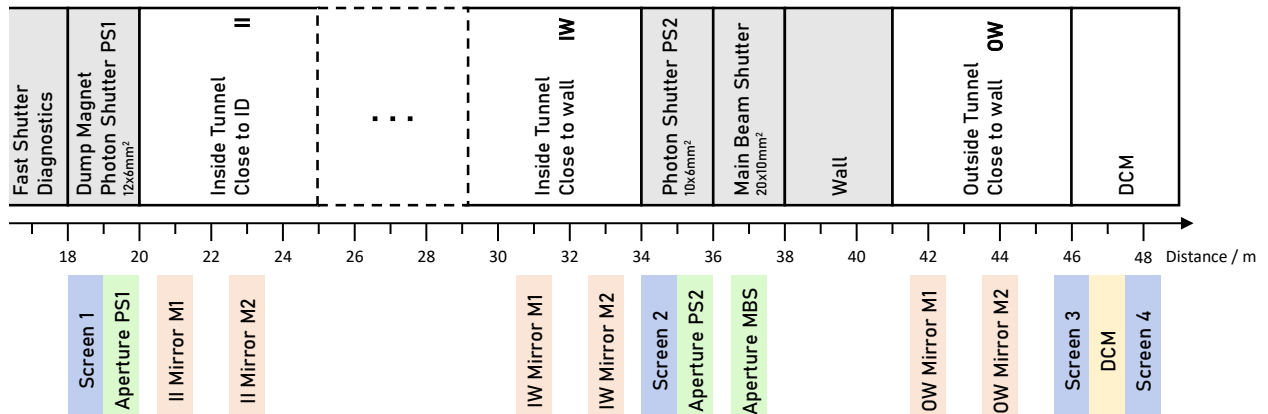
Page 14 of 44

Figure 7: Mandatory equipment within the tunnels [42] (grey boxes) and their corresponding positions. Different potential locations of (collimating) mirrors (orange boxes; see Sec. 4.6) are indicated. The bottom row describes the categories of optical elements as used in xrt.

first 20 m after the insertion device. Additionally, the last 6 m before the wall are reserved for the photon shutter PS2, the main beam shutter as well as further vacuum equipment, and diagnostic units. Furthermore, 1 m space is required for a diagnostic unit behind the wall of 1.5 m thickness. Further, the area 8 m after the dump magnet is generally kept free to avoid damage in the extremely rare case of escaping electrons, which is why we also consider an additional placement within the tunnel.

The calculations will include several aspects to evaluate different options:

- three mirror pair positions
    - II   *I*nside tunnel, close to *I*D   at 22 m and 24 m
    - (IW) *I*nside tunnel, close to *W*all   at 32 m and 30 m
    - OW   *O*utside tunnel, close to *W*all   at 43 m and 45 m
- four shapes
    - bent 1D   bent flat (vertical collimation)
    - para 1D   parabolic (vertical collimation)
    - para 2D   parabolic
    - toro 2D   toroidal
- several positions to evaluate beam size and shape, as well as flux
    - before photon shutter PS1   screen   at 19.9 m
    - at photon shutter PS1   aperture   at 20.0 m
    - before photon shutter PS2 and main beam shutter   screen   at 34.9 m
    - at photon shutter PS2   aperture   at 35.0 m
    - at main beam shutter MBS   aperture   at 37.0 m
    - before monochromator   screen   at 46.9 m
    - after monochromator   screen   at 47.1 m
    - after mirror 1 and 2 (determine optimal length and pitch)   mirror
- different lengths
    - default: maximum available length, symmetric to center point (here: 2 m)
    - five steps in reasonable range between 60 cm to 1400 cm
- different incident angles
    - 1.8 mrad, 2.0 mrad, and 2.5 mrad
- material
    - Rh
    - (Pt)

Results for AppAnaXAFS.

First of all, different mirror geometries and their effects on the beam shape are studied. Especially for small radii and long mirrors the beam shape can become very asymmetric and wide spread. Figure 8 compares the beam shapes for different mirror positions, geometries, and sizes as well as incidence angles. The exemplarily comparison includes the extreme cases of realizable settings for the incidence angles (1.8 mrad and 2.5 mrad) and mirror lengths (600 mm and

1400 mm) as well as all four introduced shapes and the two positions II and OW. In general, all combinations result in well-behaved beams with almost rectangular shape, with a slight bent for the 2D mirrors.
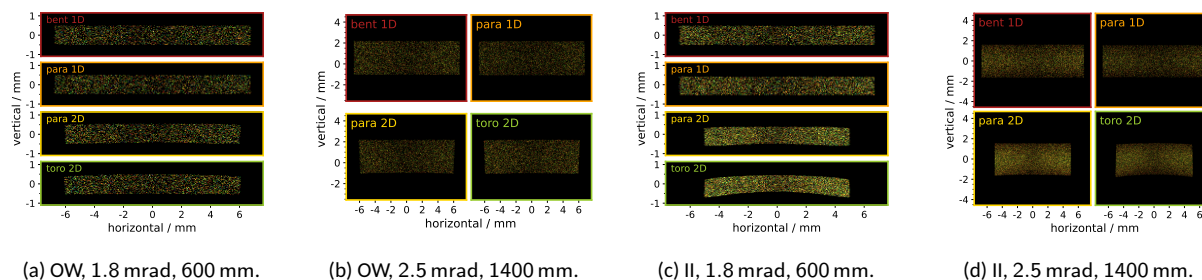
(a) OW, 1.8 mrad, 600 mm.   (b) OW, 2.5 mrad, 1400 mm.   (c) II, 1.8 mrad, 600 mm.   (d) II, 2.5 mrad, 1400 mm.

Figure 8: Overview of the effects of different mirror settings on the shape and size of the beam for different incidence angles and mirror lengths for mirrors at II position. The presented screens are located right before the monochromator at 46.9 m.

Additional detailed studies were performed to evaluate the intensity loss at different elements of the beamline in front of the monochromator for different positions of the mirrors. Figure 9 displays the flux calculated at different stages of the beamline for the mirror positions II and OW, respectively. Both subfigures consist of several panels presenting combinations of different incidence angles (columns) and mirror shapes (rows). Each individual panel presents curves for different mirror lengths (color coded), including the mirror-free option. Naturally, all variants result in a reduction of flux, primarily due to the various shutters, which are responsible for a loss of approximately one order of magnitude for the mirror-free option. For the OW position of the collimating mirror, the flux is further reduced by the interaction with the mirror surface (reflectivity of Rh at a certain incidence angle) as well as the mirror size (beam projection onto inclined surface), see Fig. 9 (a). Additionally, for this mirror position, no significant difference in flux is recorded for the different mirror shapes. Here, more sophisticated shapes (parabolic, 2D) have no advantage over the simple bent mirror.

When the mirrors are positioned between the Photon Shutters PS1 and PS2 (position II), then the collimation of the beam preserves some of the otherwise lost photons and higher fluxes than for the mirror-free calculation are possible, see Fig. 9 (b). In case of 2D mirror shapes, the losses by horizontal beam cutting at the shutters is reduced significantly. Here, the 2D shapes have the advantage of a higher flux, but this is associated with higher production cost of the mirror. In general, the intensity is at least a factor 5 lower for mirrors at the OW position. Additionally, the influence of the mirrors length is also clearly visible for both tested positions and is responsible for a intensity difference of a factor $\approx$3 to 5 between the shortest and longest mirror versions (600 mm to 1400 mm, respectively).

The final evaluation step includes the calculations of the flux and energy resolution behind the monochromator for the two energies 9 keV and 22 keV both using the Si(111) monochromator crystals, see Fig. 10. The FWHM of the 1D energy histogram (see App. A) was used to determine the energy resolution, see Sec. A.

In the case of mirrors placed at the OW position, the individual results hardly differ from each other. Generally, the flux is 2 to $4 \cdot 10^{10}$ photon s^{-1}, independently of energy and mirror shape, only slightly increasing with mirror length. In order to perform reasonable XAS experiments, a minimum flux of 10^{12} photon s^{-1} on the sample is required. To compare the experimental value and the calculated data, two things must be considered. On the one hand, the experiment includes more objects that interfere with the beam, e.g. diamond windows and air. Experience shows that these objects are responsible for the loss of intensity by a factor of 10. On the other hand, the displayed flux is the value for the entire beam, which has a size in the range of 13.5×1.1 mm^2 to 13.5×3.5 mm^2 (depending on the mirror length) at the DCM. This is the maximum flux on the sample, when a perfect focus on the sample position is possible. In reality, further losses must be expected. In summary, for mirrors at the OW position, the possible flux is too low for the intended experiments.

The energy resolution is also independent of the mirror shape and length and has values of 1.2 eV and 3.2 eV for 9 keV and 22 keV, respectively. For the mirror-free option, the values (6 eV and 23 eV, respectively,) are not presented here as they would affect the readability of the graphic.

For the mirrors at II position, the flux is always increased compared to the mirror-free option, the value is at 10^{12} photon s^{-1} and 2×10^{10} photon s^{-1} for 9 keV and 22 keV, respectively. Although, the flux for this setup is higher, it is not sufficient for the intended experiments.

The energy resolution for mirrors at II position is 1.2 eV and 2.0 eV for 9 keV and 22 keV, respectively. For the mirror-free option, the values would be 6 eV and 23 eV, respectively, and would affect the readability of the graphic.
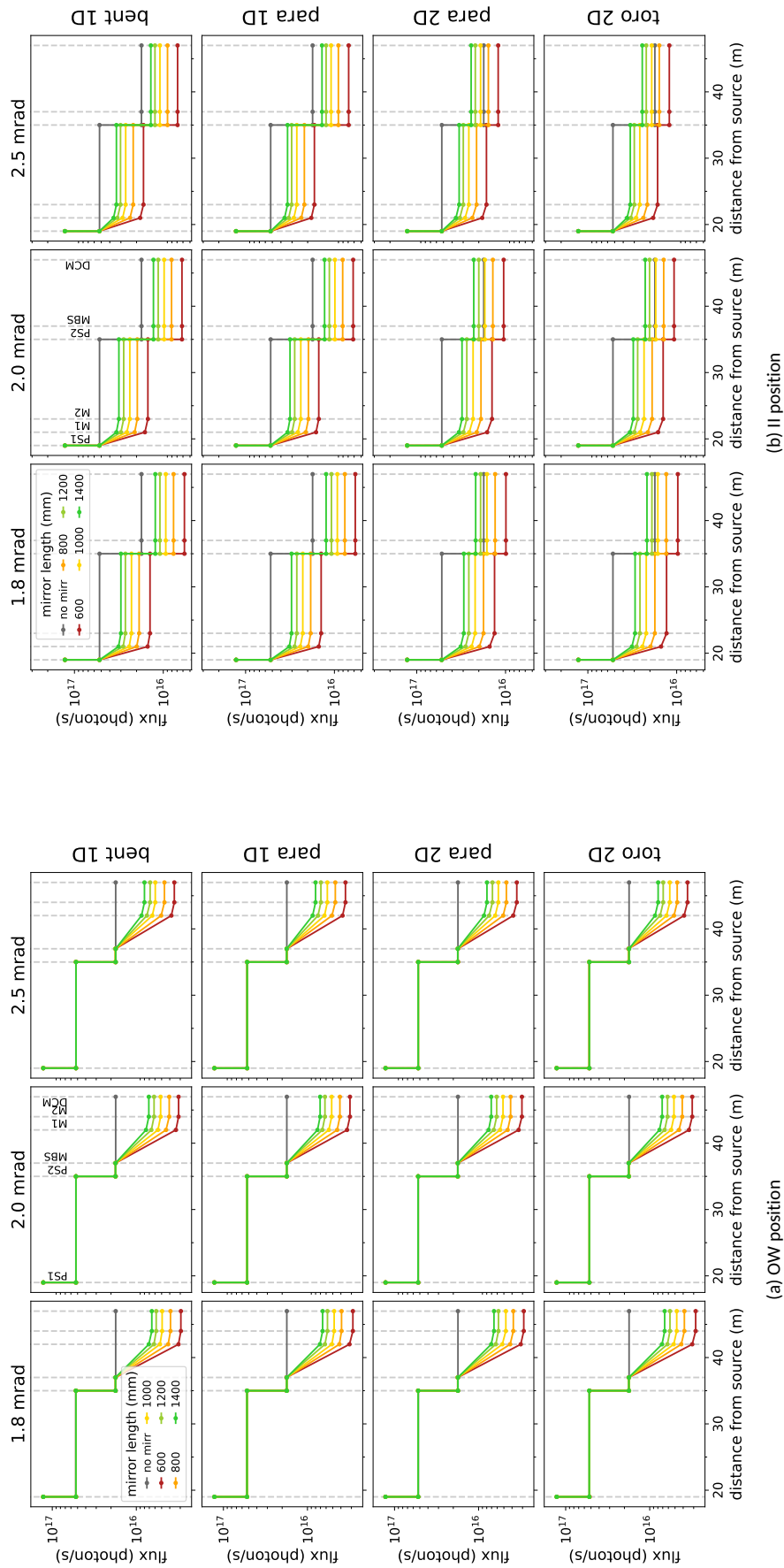
Figure 9: Flux at different stages of the beamline for different combinations of incidence angles (columns) and mirror shapes (rows). Each individual panel presents curves for different mirror lengths (color coded), including the mirror-free option. The lines serve as guide-to-the-eye for the flux development between the various calculated positions (marked with a point).
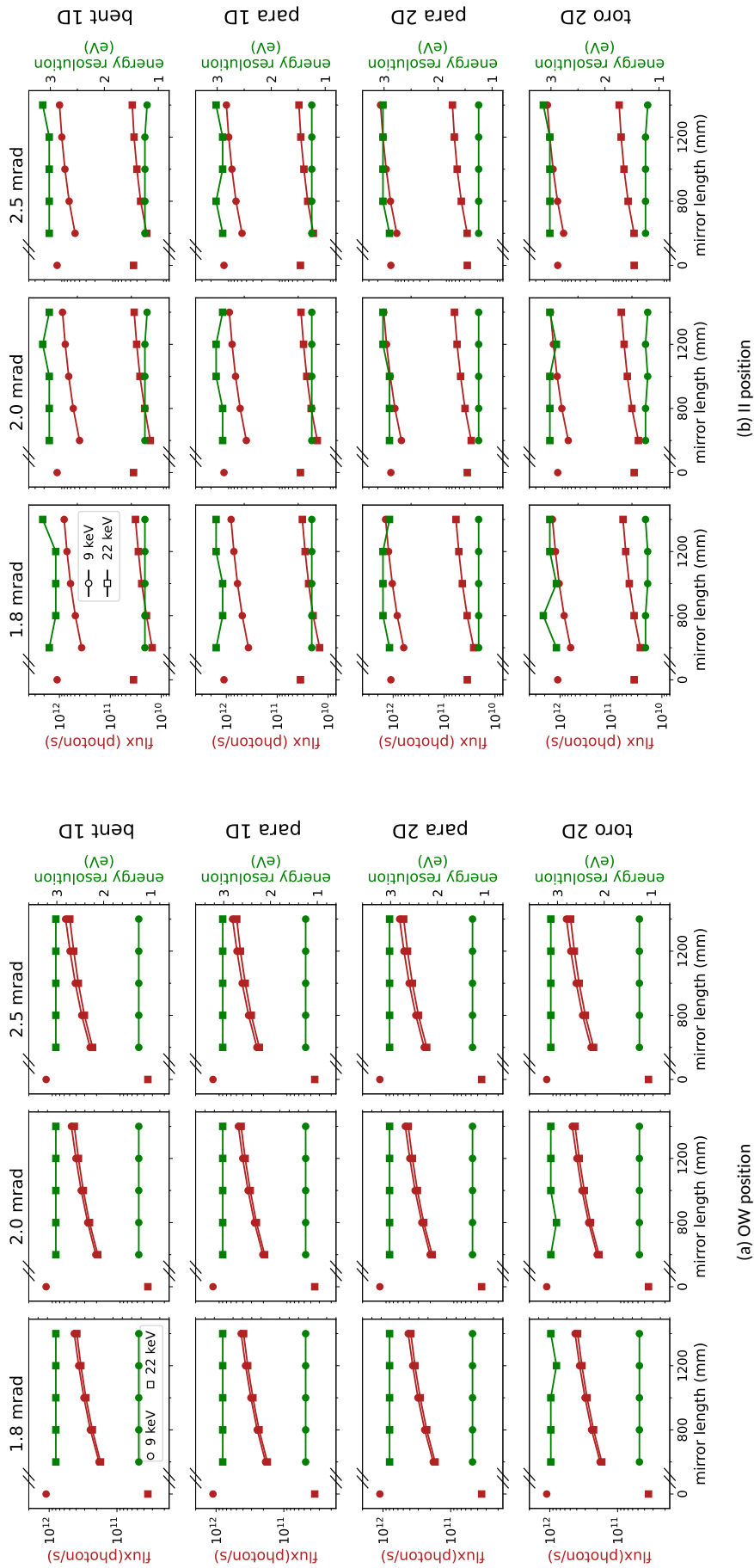
Figure 10: Flux density and energy resolution behind the monochromator for different combinations of incidence angles (columns) and mirror shapes (rows). The data of the mirror-free option is included for a mirror with a nominal length of 0 mm.

4.7. Focusing (and Collimation)

Beside the already mentioned focusing mirrors, a broad range of other focusing devices exists. The application of those devices is to create an image (with reduced size) of the source onto the sample. Geometrically, the focal length f is related to the object distance p and the image distance q by:

$$\frac{1}{f} = \frac{1}{p} + \frac{1}{q}.$$

(3)

In the case that a parallel beam is desired, the process is called collimation and $p = \infty$ [67].

Focusing devices can be categorized according to the underlying physical effect as reflective, diffractive, and refractive. The most elaborate and most flexible representatives of each group are *Kirkpatrick Baez* (KB) mirrors [69,70], *Reflective Zone Plates* (RZP) [71,72], and *Compound Refractive Lenses* (CRL) [73,74], respectively. Each of those devices offers different advantages and disadvantages. The linearly arranged FZPs and CRLS provide the easiest handling. Generally, the smallest beam can be generated with diffractive and reflective elements. Reflective optics are non-dispersive, which means that they work independently from the wavelength (energy) of the X-ray beam. In turn, this property makes reflective optics most advantageous for X-ray energy scanning, despite the disadvantages of large dimension, difficult handling, and high costs for high quality polishing.

Among the different relfective optics (*e. g.* Schwarzschild optics [75,76], Wolter optics [77]), the most favored options for synchrotron applications are a set of toroid mirrors, KB mirrors [69], and Montel mirrors [78]. The toroidal mirrors are usually free in their placement across the beamline and, as the name indicates, they manipulate the beam both horizontally and vertically. In contrast, KB mirrors come as a pair, typically after the monochromator. Both mirrors are elliptically shaped and each focuses to a line and sequentially to a spot [54]. In a conventional KB setup, the mirrors are placed successively; in order to save space and reduce offsets between the mirrors, Montel mirrors offer a more compact design [78], at the cost of more difficult polishing and manufacturing.

CRLs and RZPs are dispersive as the focal point changes with energy. By simply adapting the position of CRL (stacks) and/or changing the amount of active lenses for a new energy, the focal condition can be met again [74]. Devices designed to do just that are called *transfocators* and are still under development [79]. However, the lens material is often contaminated by transition metals, which could falsify the signal when investigating the corresponding absorption edges. Therefore, lenses made of silicon or diamond would be most beneficial, which are cost-intensive due to the material itself or because of the high computational effort to calculate the optimal shape. However, RZPs can only be used to a limited extent for energy scans by varying the incident angle [80].

Additionally, CRLs generally have a diameter of $< 5\,\mathrm{mm}$ [81, 82], which is already significantly exceeded in horizontal direction at the position of PS1 of the AppAnaXAFS beamline. And RZPs can be manufactured [83] with a usable aperture of $80 \times 20\,\mathrm{mm}^2$. For a typical incidence angle of 0.8° for hard X-rays, a vertical acceptance of $1.1\,\mathrm{mm}$ is a reasonable estimate [80], which falls significantly below the $6\,\mathrm{mm}$ beam size after PS1. This means for both cases that a major part of the photons would not be focused on the sample, which in turn results in a significantly reduced primary intensity.

In accordance with the previous discussion, all the beamlines analyzed in Sec. 3 rely on mirrors for focusing, with a majority employing KB or toroidal mirrors.

Mainly because of the large beam size expected from the 3-pole Wiggler, the mirrors are best suited for the AppAnaXAFS beamline.

4.8. Absorber

While mirrors in form of HRM (see Sec. 4.6) suppress the higher harmonics, absorber can be used to filter out low energy photons, which both facilitates to reduce the heat load on the first monochromator crystal 4.5 [84]. The operating principle is based on the energy dependent absorption of X-rays by a material: the higher the energy, the less the radiation is absorbed by a chosen material with a certain thickness. In general, it is advisable to sacrifice 10 % to 20 % of the maximum flux to reduce the thermal load on the optical components. Typical absorbers are foils made of Al and Cu of different thicknesses, as well as glassy carbon and diamond. The absorber material must be chosen wisely with regard to the X-ray energies used in the XAS scans: the absorber may not have an absorption edge within the scan range.

4.9. Experimental Hutch

The experimental hutch must offer plenty of space for placing the sample stage (see Sec. 4.9.1) as well as various detectors, sensors, and analyzers (see Sec. 4.9.2) and, additionally, the equipment to vary the sample environment (see Sec. 4.9.3).

4.9.1. Sample Stage

The main options for a sample stage are multi-circle diffractometers and optical tables. Most spectroscopic experiments are measured in transmission or fluorescence mode and do not require the highly accurate positioning of diffractometers. Instead, the surface of the optical table could be used for the flexible setup of different devices for the manipulation of the sample environment close to the sample position, see Sec. 4.9.3.

4.9.2. Detectors, Sensors, and Analyzers

In general, X-ray experiments are recorded with a large variety of detectors, sensors, and analyzers at different positions of the beamline [85]. For most spectroscopic experiments, the application of ionization chambers and diodes delivers the desired information reliably, quickly, and efficiently. The general setup is an all transmission setup consisting of three ionization chambers (plus electrometers) for the primary beam I_0, for the signal I_1 of the sample, and for the reference I_2, see Fig. 11. Depending on the selected energy, the chambers are filled with varying gases and pressures, generally heavier atoms are more suitable for higher energies [86]. The best solution for fluorescence measurements up to 20 keV is the application of a PIPS diode (Passivated Implanted Planar Silicon [61]). Unfortunately, this diode also reacts on visible and infrared photons, which makes the application in temperature dependent studies more challenging. For fluorescence measurements of complex compounds or for strongly diluted absorbers, *Silicon Drift Detectors* (SDD) are recommended [87, 88].

In contrast, 2D detectors are rarely used since most samples are in powder form, for which no spatial resolution is required [89]. In particular, Q-EXAFS scans, as envisaged for the AppAnaXAFS beamline, require detectors with a very high temporal resolution (approx. 100 spectra per second spanning approx. 1 keV with 1 eV steps resulting in 100 kHz), which cannot be permanently acquired by most 2D detectors. Currently, very

Figure 11: Stack of the electrometers recording the intensities at the ionization chambers.

high temporal resolution is achieved with Eiger2 X/XE [90] at 4.5 kHz and with Lambda detectors from XSpectrum at up to 24 kHz (with 1 bit resolution) [91]. For the Q-EXAFS applications, ionization chambers are preferred, especially the gridded versions [62, 92, 93], which overcome the drawback of slow heavy ions (used at higher X-ray energies) by collecting them and separating their signal from that of the lighter and quicker electrons [48].

The different analyzers dedicated to the catalytic experiment will be discussed in Sec. 4.9.3.

4.9.3. Equipment for *in-situ* catalysis experiment

Additional equipment is naturally necessary for characterizing the catalytic part of the experiment. The specific analyzers required vary depending on the focus of the experiment.

The future AppAnaXAFS beamline will mainly focus on gas-flow catalysis as performed *i. a.* by the Grunwaldt group at KIT [94], see Fig. 12. Thus, the following equipment is needed to record the desired *operando* data and parts of the characterization data (see Tab. 1) [44, 89]:

- heater and temperature sensors (room temperature up to 600 °C)
- access to different gases, including gas mixing [95]
  - devices for gas supply
    - most important gases: O_2, N_2, He, H_2, CO_2, CO, CH_4, (H_2O)
    - sufficiently large gas cabinets
  - devices for gas analysis
    - gas chromatograph
    - mass spectrometer
  - mass flow controller
  - flow meter
  - exhaust
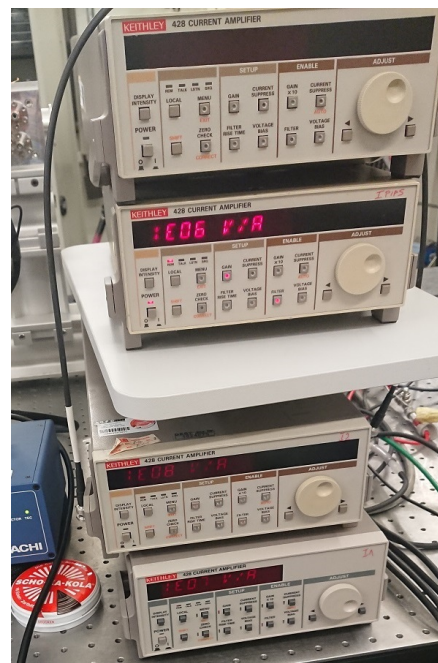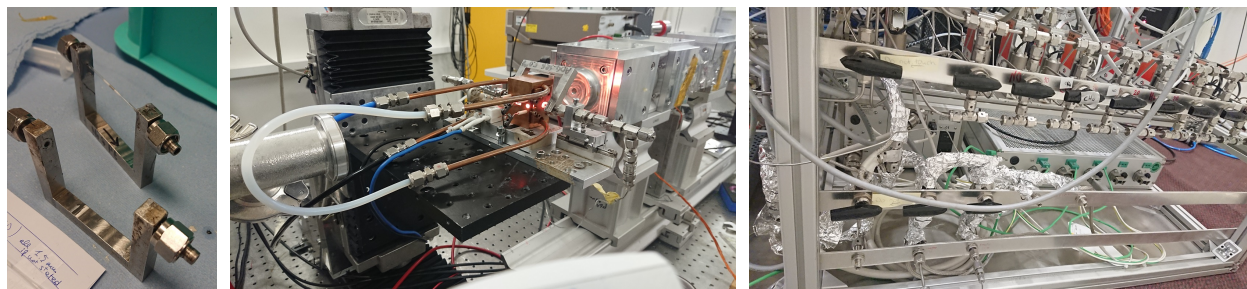 - Fourier-Transform Infrared (FTIR) gas spectrometer

Figure 12: Different equipment used by the Grunwaldt group [94] from KIT for gas-flow catalysis experiments. Left: U-shaped sample holders with and without catalyst-filled capillary. Middle: *In-situ* experiment including a resistive heater with water cooling applied to a capillary in a u-shaped holder [96]. Right: Gas mixing system for laboratory applications.

Other catalytic experiments could also require:

- syringe pump [97]
- potentiostat [97]
- solar simulator [97]
- optical filters [97]
- calibrated Si-photovoltaic reference cell [97]
- magnetic stirrer [98]
- electrometer

5. Automation and related aspects

5.1. Control systems

The details of automation strongly rely on the infrastructure provided at the beamline. The infrastructure consists of different layers including

- run engine, *e. g.*
  - Sardana [99]
  - BLISS [100]
  - BlueSky [101, 102]

- hardware abstraction, *e. g.*
  - ophyd [103]
  - tango [104]

- control system, *e. g.*
  - SECoP [18, 105]
  - EPICS [106]

In the case of PETRA IV, different options are discussed at the moment. Within the ROCK-IT project, the following constellation will serve as a preliminary test to make a well-informed decision for PETRA IV:

- BlueSky,
- ophyd,
- Tango (DESY) and EPICS (KIT) for beamline, detectors, and frontend,
- SECoP for sample environment.

The dedicated hardware abstraction layer of BlueSky is ophyd and facilitates a common base for forwarding commands to Tango and EPICS. BlueSky generates different kinds of events (*e. g.* image taken, scan ended), which can be used to trigger actions especially during online analysis, see Sec. 5.4.7.

5.2. Automation

A high degree of automation always goes hand in hand with less flexibility with regard to changes in the measurement setup. Therefore, the integration of new devices takes a certain amount of time until all functions are fully embedded, tested, and error-resistant.

The full automation of an X-ray Absorption Spectroscopy Beamline involves all steps from beamtime preparation to execution, and to data storage. Additionally, various safety aspects must be considered when planning remote and fully automated experiments, among them safety issues from the experiment (high voltages, low and high temperatures, gases, etc.) as well as cyber security while remotely accessing the beamline control system. Here, we will also briefly discuss the important auxiliary step of fully automated *ex-situ* experiments, which are already interesting for industry partners by excluding differences in human handling [107]. The challenges of automation from *ex-situ* and *in-situ* measurements are fairly different as the former focuses on high throughput at constant conditions and the latter on varying experimental conditions of a low amount of samples.

5.2.1. Automation of the beamline alignment

The alignment of a beamline, which focuses on a very specific type of measurement, always consists of the same steps and can therefore be automated very easily. Generally, the alignment involves the adjustment of energy, mirrors, and sample stage. At the AppAnaXAFS the alignment will comprise mirrors, monochromator, filters, table height, and the electrometers corresponding to the ionization chambers, see respective subsection in Sec. 4. The complete process of the predecessor beamline P65 [84] has been visualized within this project in *Business Process Model and Notation* (BPMN), see Fig. 13. Both this and all upcoming processes were designed in strong cooperation with all work packages of the ROCK-IT project [17]. The visualization and realization of the individual steps is work in progress and originally started with a focus on the experimental site. Therefore, an imbalance between level of details is present between experiment and all other aspects.

The alignment starts by choosing the appropriate energy of the XAS experiment. Depending on this energy, first the undulator must be optimized by adapting undulator gap and undulator harmonic. Next, the mirror surface (Si, Rh, or Pt) and the monochromator crystals (Si111 or Si311) must be selected according to the energy. In case that neither mirror nor crystals need to be changed, only a simple beamline alignment is necessary, involving the scans of Δ-θ (mirror angles), table height, and undulator offset. Otherwise, a finely tuned process involving the aforementioned scans as well as changing the surfaces and coatings must be executed.

Each of these steps is already well automated at P65, using multiple python-based *Graphical User Interfaces* (GUIs) that allow for a smooth transition to a fully automated alignment, which can easily be transferred to the future App-AnaXAFS beamline. However, a crucial aspect is the prediction and handling of all possible errors that could occur during a measurement, see Sec. 5.2.4.
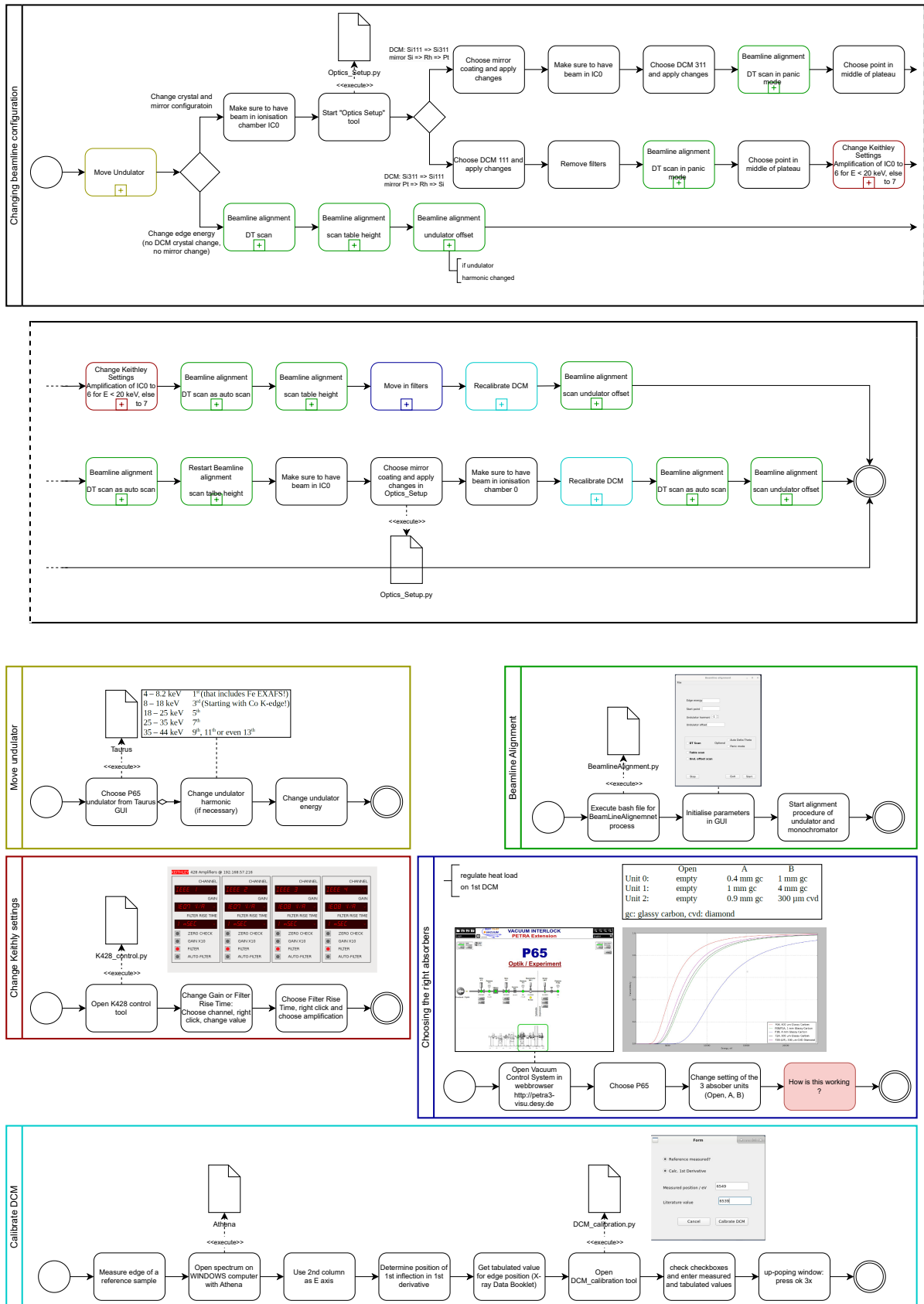
This project has received funding from the European Union's Horizon 2020 research and innovation programme under grant agreement No. 871072.

Page 22 of 44

Figure 13: The alignment steps of beamline P65, the predecessor of AppAnaXAFS, visualized with *Business Process Model and Notation* (BPMN).

5.2.2. Automation of *ex-situ* XAS measurements

After fully automatizing the alignment process, also the *ex-situ* XAS measurements must be automatized. The current process of the *ex-situ* XAS measurement at P65 is depicted in Fig. 15. The steps involve the previously discussed alignment of the beamline (see Sec. 5.2.1), the sample preparation and installation, the sample alignment, as well as the XAS measurement itself. Sample preparation and installation are manual steps. The use of sample holders that are capable of accommodating multiple similar samples is common practice for fast, *ex-situ* XAS measurements, see Fig. 14. The sample alignment basically consists of centering the sample horizontally and vertically. The XAS measurement can be performed in

Figure 14: Sample holder for nine powder-filled capillaries for *ex-situ* XAS measurements [2].

step mode or continuous mode. The major difference between both approaches is the motor movement and synchronization with the detector. While in step mode the undulator and monochromator move step by step to the precisely calculated positions and record the intensity there during standstill, in continuous mode the motors move continuously between the calculated start and end position within a specific time frame and record the intensity during the movement. In general, modern implementations of continuous scans offer the same accuracy and (often) a significantly lower overhead (amount of time needed for a scan in addition to overall exposure time) and thus higher efficiency.

Generally, the size of the energy steps is adjusted for each measurement in order to achieve a balance between information gain and time expenditure. Finer steps are necessary for the edge region, while wider steps are used in the pre-edge region and especially in the far post-edge region [89]. Often, a previously prepared table can be used as input for energy steps and integration time instead of the data input with a GUI.
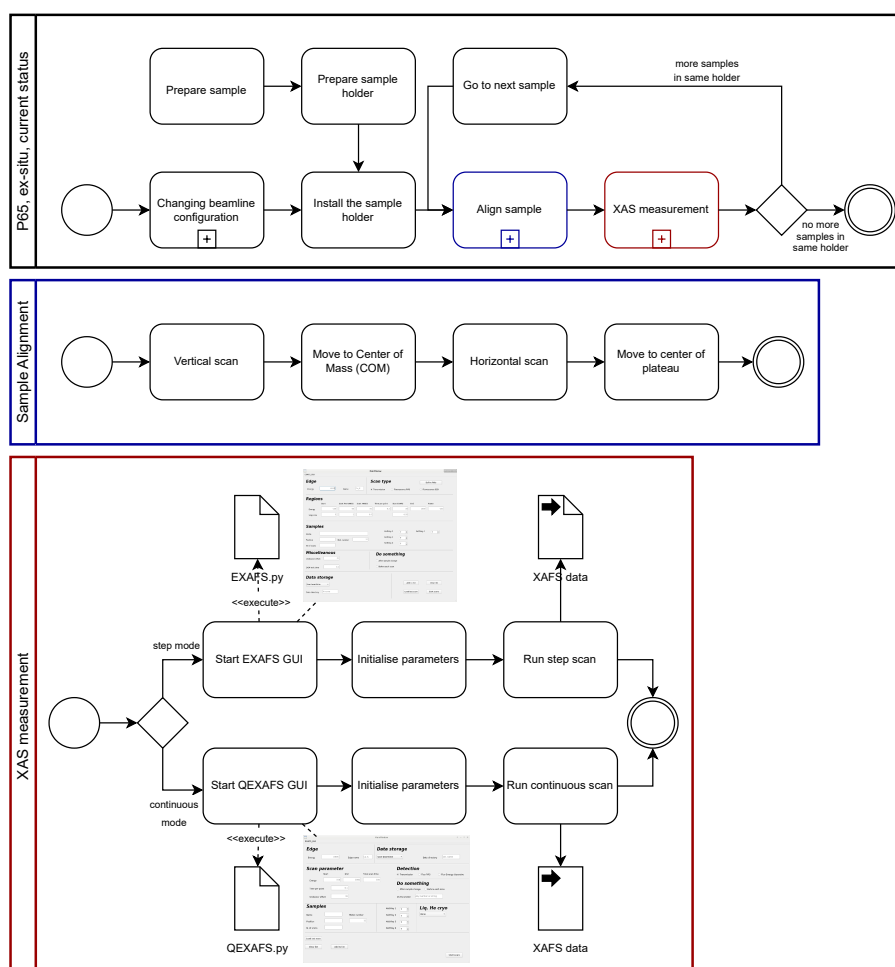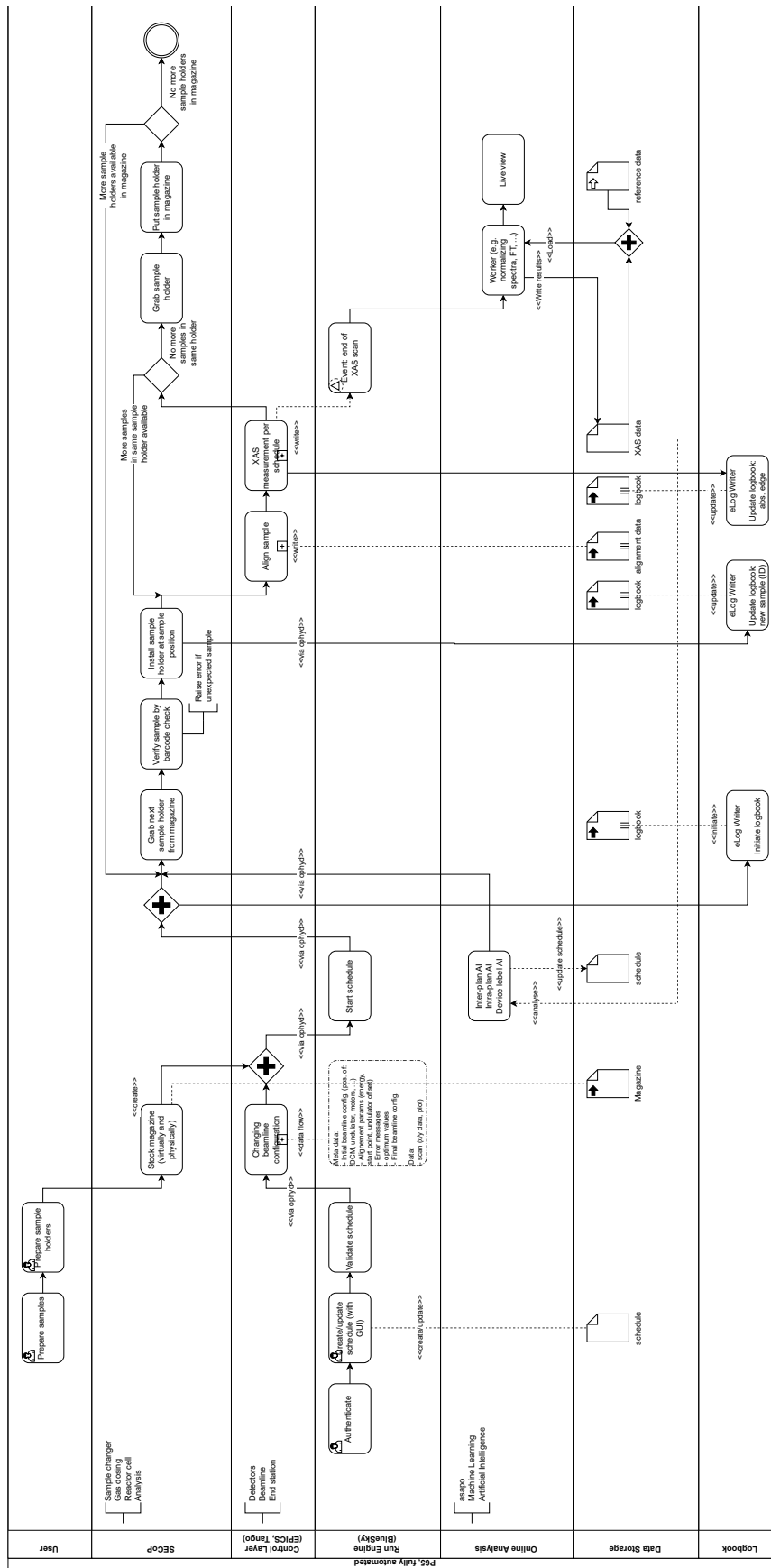

Figure 15: The current steps of an *ex-situ* XAFS measurement at beamline P65, the predecessor of AppAnaXAFS, visualized with *Business Process Model and Notation* (BPMN). The procedure to change the beamline configuration is depicted in Fig. 13.

High-throughput *ex-situ* XAS measurements are of high interest for the industry to analyze large quantities of samples, *e. g.* with slightly differing growth conditions [107]. Further requirements (on the part of the industry) are necessary for this type of measurement:

- automated sample changing
  - large sample amount available: many slots in sample holder and/or automated exchange of sample holders (robot needed), see Sec. 5.2.3,
  - supply of a magazine (storage for sample holders),
- error handling to facilitate uninterrupted, autonomous measurements, see Sec. 5.2.4,
- cyber security
  - secure authentication of remote users, see Sec. 5.3,
  - secure data storage and exclusive data access from original users, see Sec. 5.3 and 5.4.1,
- automated and unified data storage
  - data storage at the research facility, see Sec. 5.4.1,
  - standardized data formats, see Sec. 5.4.2,
  - automatized export to metadata catalog, see Sec. 5.4.3,
  - automatized *Electronic Laboratory Notebook* (ELN), see Sec. 5.4.4,
  - unique sample identification, see Sec. 5.4.5,
  - XAS database, see Sec. 5.4.6,
  - on-line data analysis, see Sec. 5.4.7,
- unification and standardization
  - standardized processes following DIN or other norms,
  - loading and validation of a predefined measurement schedule.

After including all these tasks, the process of the beamline will be significantly more complex, see Figs. 16 and 17.

Figure 16: The future vision of fully-automatized *ex-situ* XAFS measurement at beamline P65, the predecessor of AppAnaXAFS, visualized with *Business Process Model and Notation* (BPMN).
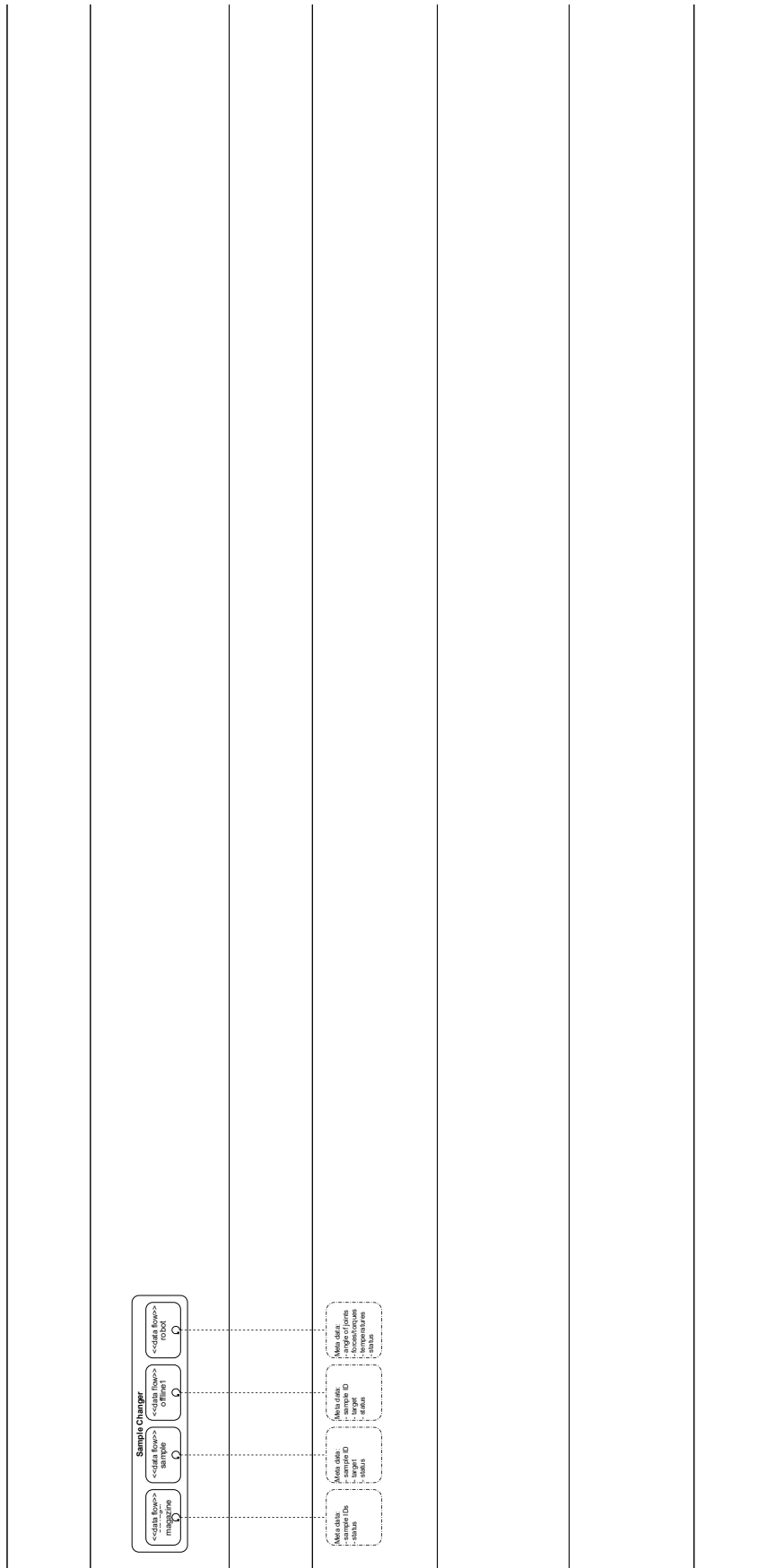
Figure 17: Readback values and metadata from different devices for a fully automated *ex-situ* measurement.

This project has received funding from the European Union's Horizon 2020 research and innovation programme under grant agreement No. 871072.

Page 27 of 44

5.2.3. Automatic Sample Exchange

Using robotic arms in fully-automated catalysis experiments as a sample changer offers several advantages, especially for synchrotron applications. Firstly, they can be operated remotely, even when working in (potentially) dangerous environments, *e. g.* under the influence of radiation and under exposure to hazardous chemicals or reactions caused by the catalysis experiment itself or by gas leakages. However, only so-called collaborative robots are capable of working in close proximity to humans and together with them. For other robot variants an additional interlock of the experimental hutch is required that switches the robot off while people are present. Additionally, they are programmable, which improves productivity by facilitating continuously ongoing experiments independently of nights and weekends. Furthermore, the programmability also allows for remote

Figure 18: Robotic arm "in training" for heterogeneous synthesis of potentially functional materials at KIT [108].

experiments and the integration of the robot into a larger process of individual (scheduled) analysis steps. By integrating a QR code scanner (camera) into the beamline setup and labeling the samples with QR codes including a sample ID, the verification of the correct sample selection from the magazine (storage) is possible in real time. However, these advantages come at high costs for acquiring and maintaining robotic arm systems. Additionally, the operation of these arms requires specialized training and expertise, as well as significant time and effort initially. Fortunately, for beamline P65 and the future AppAnaXAFS beamline, this knowledge is already available within the ROCK-IT project. Although robotic arms are not suitable for decision-making, the careful integration of machine learning and artificial intelligence into the online analysis tools can take over part of this task. As the robots are limited in terms of range of motion, dexterity, and handling delicate materials, it is not possible to let it change capillaries in the currently used u-shaped sample holders, see Fig. 12. Instead, the design of a smart sample holder system is needed that could serve as prototype for a future standardization of gas-flow sample holders. This new design includes one part, which situated at the sample position and connected to the gas-mixing system, and a second part, which includes the capillary. The robot is now supposed to grab the movable part from the magazine and attach it to its fixed counterpart, facilitating the gas flow. A cheap and easy design is already discussed within the WP3 of the ROCK-IT project.

5.2.4. Exception Handling

One of the biggest challenges in automation, apart from implementing the ideal algorithm, is dealing with unforeseen events: exception handling. In the presence of a user or staff member, these issues can be solved by intuition or experience. However, in automated experiments, these exceptions must already be considered by turning this experience and intuition into scripts. Generally, exception handling consists of three parts: error detection, error correction, and error notification. For a fully automated beamline, all arising errors are handled at best, regardless of whether they are expected or unexpected. For unexpected errors this mostly means that the experiment is stopped in a save way for man and machine and that notifications are sent to users and staff as well as to the log.

Some expected errors are already considered in the presented BPMN schemes and appropriate actions are mostly simple to implement, for instance:

- gas leakage
    - → most probably due to broken capillary, use next sample
- invalid schedule (created by user)
    - → user has to adapt the schedule
- virtual and physical magazine are not identical
    - → recreate virtual magazine with robot
- (half) empty gas bottles,
    - → staff needs to refill/exchange bottles
- no intensity
    - → check PETRA status
        - → no beam: wait for beam, hold catalytic condition OR continue with catalysis experiment (users' choice)
    - → beam shutter open? (must be open)
    - → all vacuum parts marked green? (should be)

$\rightarrow$ if all previous are ok: check intensity in IC0

$\qquad \rightarrow$ scan mirrors

Other errors can be malfunctions or failures of the devices, *e. g.* if a temperature controller no longer works. With the analyzers in particular, a simple comparison between the set and actual values could reveal the error. Unfortunately, rectification involves manual work and leads to an interruption in the blasting time. For other devices, suitable strategies must be developed to detect their failure, the handling will certainly identical.

Additionally, the online analysis could detect strong deviations between selected reference and the actual measurement data, which could point on a variety of different errors, *e. g.* wrong sample composition, wrong temperature. In this case, a repetition of the recipe with the same or a provided reserve is recommended in order to verify the results.

5.2.5. Automation of catalytic off-line experiments

The default catalytic experiments at P65 are based on off-line (laboratory) experiments of gas catalysis. This involves reacting a metallic catalyst (within a capillary) with various gas mixtures at different temperatures. In order to analyze the chemical processes, control gas flow and temperature, the equipment in Sec. 4.9.3 is needed. An overview of the steps involved in catalytic off-line experiments is given in Fig. 19. After checking the gas storage and starting the measurement software for temperature and gases, the treatment plan (recipe) for the sample is loaded. Typically, the recipe for the sample treatment is listed in a table, in which the duration of the individual steps as well as the temperature and the settings for the gas mixture and flow are specified. After realizing the complete recipe, the measurement software are stopped.
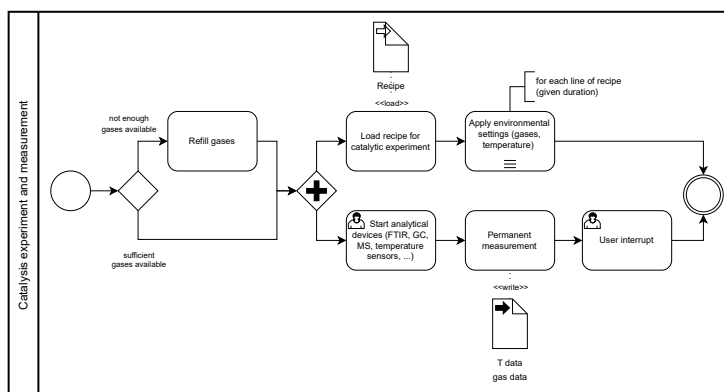
Figure 19: The steps of off-line catalytic experiments visualized with *Business Process Model and Notation* (BPMN).

The automation of catalysis experiments requires special care, not only because the capillaries tend to break and, thus, the preparation of spare samples is always recommended. Further, the heater as well as the gas supply involve some risks. Proper safety precautions must be guaranteed, especially as it is known from experience that around 10 % to 20 % of the prepared capillaries are leaky and leak checks are therefore extremely important. Additionally, the heater setup must also be safe, as it may be operated at temperatures of up to 500 °C or even 900 °C for gas blowers or resistive heaters, respectively [2], see Fig. 12.

5.2.6. Full Automatization of *in-situ* XAS experiments

In addition to the setup of *ex-situ* XAS measurements of Sec. 5.2.2, the catalytic *in-situ* XAS measurements involve additional equipment as listed in Sec. 4.9.3. In case of beamline P65, this involves a heater and gas-mixing equipment as described for the off-line experiments in Sec. 5.2.5. The accurate placement of different equipment is crucial to facilitate the measurement of all necessary information. For example, in order to record the fluorescence and transmission signal during a heated gas-flow experiment, the u-shaped sample holder should be roughly perpendicular to the beam direction. Thus, the gas mixing in- and outlets do not cross the beam path during the transmission. By placing the holder at an angle to the beam, the simultaneous fluorescence experiment is possible with the fluorescence detector in 90° angle to beam. Now, the heat blower may be placed below the capillary holder, see Fig. 12.

Currently, gas flow experiments at DESY require a person to be present at the beamline to handle potential gas leaks. In order to allow fully automated catalytic gas-flow experiments, these safety measures must be reconsidered, depending on kind and amount of gases involved in the experiment. During state-of-the-art experiments, the size of the gas bottles is often not sufficient to fill an entire experimental hutch and thus to pose a real danger.

The scheme of the full automatization of *in-situ* XAS experiments is displayed in Fig, 20. In addition to automated *ex-situ* measurements, the functionalities of the gas dosing, the reactor cell, and the analysis were added.

Figure 20: The steps of the fully automated catalytic XAS measurement visualized with *Business Process Model and Notation* (BPMN).

Figure 21: Readback and meta data at the fully automated catalytic XAS beamline visualized with *Business Process Model and Notation* (BPMN).

5.3. Remote Access, Access Rights, and Cyber Security

Remote Access is not only an important feature for mail-in experiments, but also error handling by staff members in fully-automated measurements and also for data-download by users. However, it also raises concerns about different aspects of cyber security. The major goal is the protection of computer systems and networks from attacks by malicious actors that may result in unauthorized information disclosure, theft of, or damage to hardware, software, or data, as well as from the disruption or misdirection of the services they provide.

The following measures are takes as standard:

- **Data protection:** encryption protocols and secure communication channels
- **Access control:** authentication mechanisms involving multi-factor authentication and strong passwords
- **Network security:** potential threats like malware, hacking attempts, or denial-of-service attacks; measures: firewalls, intrusion detection systems, security audits
- **Device security:** security at both remote and experimental site; software updates, antivirus software, password policies
- **Monitoring and logging:** monitoring of remote access activities; track who accessed and applied which changes
- **Training and awareness:** training on cyber security best practices

At DESY, different roles are assigned to users via two different services. Beamtime users need to have a DOOR account (*DESY Online Office for Research with Photons*) [109], which provides access to the proposal submission, declaration of substances, registration of participants, the online safety training, experimental reports, feedback questionnaire, and the data download portal (gamma portal [110]). Further, they can also have a DESY account, which gives them additional access to further services, like the Maxwell compute cluster and the Helmholtz AAI infrastructure.

The roles of participants, associated with a certain beamtime, are Principal Investigator, Leader, Participant, and Collaborator. These roles have different read/write permissions on the collected data. Additionally, each beamline has a functional account that allows full access to the data and controls of the current beamtime, but not to any other to prevent the access of a new user group to the data of a former group. Dedicated scripts ensure the smooth start and termination of a beamtime, including various saving, reset, and cleaning steps, *i. a.* the movement of the data from the local `current` folder to the dedicated folder on the central storage labeled with the respective beamtime ID.

The functional account is also used for the control of remote beamtimes. To gain remote access for a beamtime, the user must meet the same requirements as for a standard beamtime (valid DOOR account, scheduled beamtime, safety training) as well as the permission of the beamline staff, which is only granted for experienced users at the moment. The remote access can be activated by the Principal Investigator of the proposal when registering the users in DOOR as follows.

5.4. Data Storage and Data Handling

Since 2018, the European and worldwide politics has been strengthening the role of open data. In this context the term FAIR data was coined, as abbreviation for **F**ind-able, **A**ccessible, **I**nter-operable, and **R**eusable data [111]. The compliance with these principles will

- improve and accelerate scientific research,
- increase the engagement of society, and
- contribute significantly to economic growth [111].

In order to realize those principles, the DAPHNE project [20] was founded to set standards on workflow (supported by online logbooks), to establish community storages and data bases, as well as to develop and deploy user-developed analytics software for all users.

The future AppAnaXAFS beamline will provide (meta)data in different ways: as raw data wrapped in NeXus files (based to hdf5 [112], see Sec. 5.4.2), within a metadata catalog (see Sec. 5.4.3), and as a *Electronic Laboratory Notebook* (see Sec. 5.4.4). Additionally, all created data will be stored within a logfile. Most importantly, the NeXus files will assemble not only the XAS output as it is currently done, but also corresponding data dedicated to the catalysis experiment, which are currently controlled and stored at users' laptops. Additionally, the beamline control will offer an interface to update the sample information, see Sec. 5.4.5. Further, the recorded spectra could be shared in a XAS database, see Sec. 5.4.6.

5.4.1. Data Storages

The experimental data is currently stored in three different layers at PETRA III [113]. New data is directly stored to the *beamline filesystem* (BL-FS; SSD) and with short delay to the GPFS-core (disk), where it stays for 180 d for post-

processing and analysis. After this dwelling time the data is sent to the dCache (tape), where it can only be re-accessed after a staging request. The current plan is to store the data for a maximum of 10 years, as required by the *Deutsche Forschungsgemeinschaft* (DFG).

Additionally, all organizational data are stored in DOOR platform, see Sec. 5.3.

5.4.2. Data Formats

An important aspect when selecting suitable data formats is ensuring **interoperability**. On the one hand, the catalysis data should be directly linked to the simultaneously recorded XAS data, which can be guaranteed by NeXus data in particular. On the other hand, the state-of-the-art software for the visualization and analysis of XAS data, ATHENA [114], unfortunately does not yet allow the import of NeXus or hdf5 data, but rather accepts the *xafs data interchange format* xdi [115]. In order to follow modern data standards and allow further use of standard software, either the import possibilities of ATHENA must be extended or a fast conversion tool between xdi and NeXus must be provided.

NeXus data files [116] are based on hdf5 standards [112] and serve as containers including different components in a tree-like structure. These components are by default:

- NXinstrument (beamline details),
- NXsample (including composition, temperature, electric field, magnetic field, pressure field),
- NXtransformations (define order of motors at beamline),
- NXdata (plottable data),
- NXcollection (gather any set of terms, originally: description of beamline),
- NXprocess (document event of data processing),
- softlinks to external data.

At PETRA III, the NeXus Component Selector is already established, which allows the selection of different signal channels by users and staff on the fly during the beamtime. These channels can be detectors and motors, but also external data and sample details.

The recommended file size is about 30 GB, as it represents a good balance between reasonable loading/opening time (large files) and folder opening times (many small files). In addition, the minimum blocked space on the disk is 256 kB, so smaller files will not save space. And finally, the risk of interrupted downloading/copying processes is tolerable.

5.4.3. (Meta)data Catalog

In order to facilitate the FAIR principle, the recorded data must be **findable**, which can be enabled by the (automatic) metadata upload to a catalog. Currently, several metadata catalogs exist

- ICAT [117],
- SciCat [118],
- sampleDB [119].

In the framework of the PETRA IV, ROCK-IT, and DAPHNE4NFDI projects, SciCat is the preferred solution. Therefore, the partners within DAPHNE4NFDI are working on expanding the functionality of this catalog. Further, the ROCK-IT partners are currently implementing tools for the automated upload of the metadata from completed scans, either in near-realtime or shortly after the end of the beamtime. These tools have already been tested at beamline P08 within the DAPHNE4NFDI framework [21].

The exact choice of metadata to be transferred for XAS *in-situ* and *ex-situ* measurements is not yet finalized, however some of the most important keywords are:

- details about participants,
- research center and beamline of experiment,
- time period of experiment,
- sample PID, see Sec. 5.4.5,
- sample composition,
- absorption edge,
- temperature (range),
- gas flow parameters.

5.4.4. Electronic Laboratory Notebooks

During the measurements, the progress is recorded in notebooks, aside with possible trouble shootings, open questions, and preliminary insights. In most cases, the recorded data is not **reusable** if the corresponding notebook is not available. The requirements for *Electronic Laboratory Notebooks* (ELN) include

- collaborative work
  - access from different computers in parallel
  - access of several users in parallel
  - display of changes in real-time
- import of data sniplets
- text
- graphics (screenshots)
- tables
- secure access
  - collaborators identical with beamtime users

- remote access
- logs/changes associated with user
- safe cloud space

- default properties for each log entry
  - time stamp
  - editing user

Further constraints on ELN within the framework of fully-automated beamtimes are:

- **Finalization of ELN at the end of beamtime.** Especially when investigating "hot topics", it is important to be the original discoverer of a breakthrough, which can only be accomplished if the ELN is unalterable once the beamtime ends. Additionally, it must be clear, whether changes and deletions in the logs are valid and how long after creation. Perhaps all changes should be tracked.

- **Automatic generation of majority of logs,** while still allowing manual editing. Therefore, the chosen ELN solution must offer an appropriate interface, which is often not the case for proprietary software.

- **Clearly defined set of transmitted (meta)data**. The developers must decide on a set of relevant keywords, which can be transmitted. Perhaps the user is allowed to (de)select certain properties. Possible keywords are

  - absorption edge (*e. g.* Cu K),
  - time stamp,
  - editing user,
  - scan numbers,
  - temperature,
  - gas flow.

- **Size limitation.** As the ELN will be stored in the synchrotron storages along with the raw data, a limitation of the ELN size is recommended to prevent unnecessary additions from the users. The integration of image compression during upload could be helpful.

Currently, several different solutions exist ($*$ proprietary):

- Google docs [120]
- eLabFTW [121]
- SciNote [122]
- openBIS [123]
- CERF [124]
- Chemotion [125]
- NOMAD Oasis [126]
- Colabra$*$ [127]
- Labfolder$*$ [128]
- LabTwin$*$ [129]

5.4.5. Sample Database

Most existing material databases focus on a certain material as a group of samples, but not on the individual samples. However, a complementary database documenting the growth and treatment procedures is highly beneficial to identify origins in different behavior and also to link the results of different analysis methods to the same sample or sample twins. Further, such a database facilitates the application of data mining and machine learning (by making data **findable** and **reusable**) for a large variety of scientific questions like successful catalysts, experimental conditions, reaction mechanisms, and characterization techniques, as well as sample design and optimization. Additionally, most material databases focus on (more or less) homogeneous materials, although a sample could be a complicated stack of different layers, *e. g.* in solar cells and batteries. Overall, building up a sample database promotes efficient research, collaboration, knowledge sharing, and accelerates the development of improved catalysts for various (industrial) applications.

Finally, the creation of a sample database also means the establishment of a global *Persistent IDentifier* (PID). Independent from the advantages of a sample database, a sample identifier is of great importance for mail-in and remote beamtimes, especially in case of high-throughput experiments, in order to prevent confusion about the sample characteristics. Often, the sample identification is attached with a QR code sticker to the sample or sample holder.

However, the design of a sample database comes along with many questions, which are also discussed within DAPHNE-4NFDI:

- What is a sample?
  - more than just the composition
  - It is what happened to the sample: preparation, polishing, characterization, . . .
  - Does a new treatment step change the sample (PID)?
- What is a (minimal) sample description?
  - state
  - composition
- How to integrate sample relations?
  - split one physical sample in several part $\rightarrow$ siblings
  - different treatment of siblings
  - different samples with same history

After these questions are clarified within the scientific community, information must also be automatically be imported to the sample database during the measurements at P65. Currently, this step only has a low priority within the ROCK-IT project.

5.4.6. XAS Database

In the field of XAS, data are often assessed by comparing them to reference spectra that have been previously measured or calculated. Therefore, a database with reliable reference spectra is a crucial tool for analysis. This database must also contain the basic information on the experimental conditions, *e. g.* temperature, pressure. Additionally, it must be easy to use not only for providing **findable**, starkaccessible and **reusable** data, but also to encourage users in providing data by including an intuitive upload form.

The most important and difficult task might be to decide, which of the spectra to export. The most simple ways would be to export all or none, which would either contradict the FAIR data storage or would require too much storage space. Therefore, the upload must either be manual or underlie and intelligent online analysis and evaluation, see Sec. 5.4.7.

Currently, several XAS databases exist in parallel and a unification would be desirable:

- XASLIB [130],
- XAS database [131],
- AcReDaS [132],
- The Materials Project [133],
- XAS reference database under DAPHNE4NFDI [134].

Currently, the data upload to a XAS database has a low priority within the ROCK-IT project and will not be realized there. However, DAPHNE4NFDI is focusing on this subject.

5.4.7. On-line Data Analysis

In order to supervise the experimental progress, the collected data is analyzed in near real-time in order to make informed decisions for optimizing the research outcomes. This so-called *On-line Analysis* strongly depends on the performed experiment and may involve techniques such as image reconstruction, spectral analysis, pattern recognition, and statistical modeling. In case of catalysis XAS measurements at P65, the available signals for analysis are X-ray intensities as well as the set and current values for temperature and gases. Online data analysis involves processing and interpreting these values immediately after acquisition to allow informed decisions on about subsequent measurement steps in order to significantly enhance the efficiency and productivity. These informed decisions can either be performed by human users (remote and mail-in) or by artificial intelligence (full-automation). In case of fully-automatized measurements without human interference, the performed evaluation steps are still extremely helpful for final data processing and result interpretation, although a real-time analysis is not necessary in this case.

In general, some tasks of the on-line analysis can be very demanding, especially when 2D detector frames are corrected and rewritten. In such computing-intensive cases, the handling of the data flow must be organized carefully in order to guarantee that new experimental data can still be recorded. Therefore, a balanced solution must be found between fast access to the BL-FS, which could affect the acquisition of new data, and access to the GPFS-core, which is safe from data loss but slower.

The partners within the ROCK-IT project are already developing the following functions for the DESY online analysis tool ASAP::O [135]:

- normalize spectrum (signal I_1 by primary beam I_0: I_1/I_0),
- calibrate energy (foil I_2 vs reference from database),
- visual comparison to reference data,
- automatically saving normalized spectra from I1 and PIPS as png,
- linear combination analysis (of normalized signal using reference data from several related compounds),
- *Fourier Transformation* (FT) of the spectra,
- *machine learning* (ML) algorithms to change the measurement schedule.

The last point could be realized such that the change is applied during next iteration (inter-plan) or while schedule is running (intra-plan). While the former approach is more easy to realize, the latter makes experimentally more sense. Possible improvements by ML could affect

- energy resolution of XAS scan (more information vs higher time resolution),
- temperature ramps or holding times in catalysis experiment,
- gas flow in catalysis experiment.

However, to apply ML algorithms, a sufficiently large amount of training data is required. In order to provide the data, the following steps are helpful:

- **data mining** from existing data bases, not only including XAS data, but also environmental parameters on the catalytic experiment,
- **access to DESY storage**, although the data protection policy possibly restricts this and the assignment of the correct catalytic parameters could be challenging.

Additionally, future users could be asked when starting the beamtime, if they would provide their data for ML training with a simple checkbox.

Depending on the time resolution of the Q-EXAFS scans, real-time visualization will only be able to display the latest finished scan, but not all of them.

6. Conclusion

This report discusses several design choices for a fully-automated *in-situ* XAS beamline, covering not only the physical beamline layout, but also detailed considerations on required automation steps. The physical layout was discussed for the future PETRA IV beamline AppAnaXAFS, which will be the successor of PETRA III's P65. For this beamline Q-EXAFS measurements are desired, based on a 3-pole Wiggler with a large divergence. Several options for collimating mirrors have been discussed in this report, especially covering two different positions within and outside the tunnel. However, all versions lead to nominal fluxes of less than 10^{12} photon s^{-1} that would be needed on the sample to perform the measurements. Therefore, the application of the 3-pole Wiggler for AppAnaXAFS is not recommended. For the intended Q-EXAFS measurements this means that either a tapered undulator must be employed or these measurements are strongly limited in temporal resolution. However, this conclusion comes with the advantage of a simpler beamline layout:

- The 3-pole Wiggler can be replaced with a standard undulator.
- The collimating mirrors close to the ID are not required anymore (Only one focusing mirror is required, complemented by a flat mirror.)
- A Q-DCM is not required.

In total, these changes also imply a strong reduction in cost for this beamline.

The second part of this report comprises detailed discussions on necessary automation steps and option. A major achievement within this project is the assembly of several process charts visualizing the individual steps during a fully-automatized *in-situ* XAS beamtime, not only from the experimental perspective, but also including the data flow. This chart has already become very extensive, but is still work in progress and will be further refined within the ROCK-IT project. Within the ROCK-IT project, the process charts are an essential basis for the communication and synchronization between the individual working packages.

7. Acknowledgements

This project has received funding from the European Union's Horizon 2020 research and innovation programme under grant agreement No. 871072.

Page 38 of 44

A. Appendix: X-ray tracing with xrt

A.1. General Remarks

The python package xrt is a software library for ray tracing and wave propagation in the X-ray regime [38]. This module is primarily meant for modeling synchrotron sources as well as beamlines and is thus predestined for the evaluation of different mirror settings of the upcoming AppAnaXAFS beamline for PETRA IV. The script generated for this report are available at [39].

xrt provides different classes of objects corresponding to different physical objects of a beamline like IDs, optical elements (monochromators, mirrors, lenses, zone plates, etc.), and apertures, as well as screens working as virtual 2D detectors. From each of these classes, several specialized subclasses are provided. For instance, the following subclasses for IDs are provided within the xrt GUI:

- `GeometricSource`,
- `BendingMagnet`,
- `Undulator`.
- `MeshSource`,
- `Wiggler`,

However, none of these classes is suitable for adequately describing a three-pole wiggler. Instead, the subclass `SourceFromField` was used to load the magnetic field (see Fig. 4) of the recommended wiggler from the PETRA IV team [52].

Further, also different classes for curved mirrors exist, covering the required geometries within this study:

- `BentFlatMirror`,
- `ToroidMirror`,
- `ParabolicalMirrorParam` (isCylindrical=True for 1D and False for 2D).

Unfortunately, these classes do not allow infinite distances to the focal points, instead a large, but finite number, namely 1×10^{18} mm, was used to create collimating mirrors. In order to ensure the redirection of the beam towards sample position a second mirror is needed, with the same incidence angle, which is realized by `pitch` in xrt, but rotated by 180° (`extraPitch`). As the second mirror is only intended to deflect the beam, it is designed as flat (`OE`), with the same length as the first one.

The use of several screens along the beamline to monitor the beam status is highly recommended. In many cases, the same information can also be obtained by analyzing the local or global beam of a physical object. However, by using screens directly in front of and behind such an object, it becomes clear whether a beam has already passed the object or not.

Further, the proper definition of the physical size of the objects is crucial, especially for the present task of evaluating whether the beam of the 3-pole Wiggler is suitable for Q-EXAFS experiments. This is especially true for the apertures, mirrors, and the DCM.

Moreover, changing the position of an xrt object is not a simple task as it does not only include updating its `center`, but also making sure that the beams are also transferred between the objects in the correct order. On the one hand, when using the GUI, a drop down menu normally contains all available beams. However, sometimes the internal update mechanisms fail and a beam is lost, which often means that the complete file must be recreated. On the other hand, adapting the python code directly, means to manually update all details. This also gives the freedom to use shorter beam names. However, some name space conventions seem to exist that could also corrupt this process.

Above all, the information content of the calculations can be improved by a large amount of `GoodRays`, which are the – in simple words – photons visible at a screen. These `GoodRays` must meet several conditions, *e. g.* they must have a valid energy and may not be blocked by an aperture. Several options exist to increase the number of `GoodRays`:

- increase the number of total rays `nrays`,
- increase the number of repeats,
- decrease energy range defined by `eMin` and `eMax`,
- decrease considered divergence of undulator `xPrimeMax` and `zPrimeMax`.

While the first two options increase the calculation time, the other two make sure that only valid photons are created and do not affect calculation time.

A.2. Plots

The most useful information for the present study are delivered by the plots of different beams associated with an physical object along the beam or with a screen. These plots mainly provide a four-part figure containing different histograms describing the beam, see Fig. 22. The three 1D histograms describe the energy as well as flux distribution in x and z direction of a selected screen, respectively. In addition, the center and FWHM of these 1D histograms are presented. The last histogram is displaying the beam shape in 2D (x and z axis of the screen). In the given example,

the beam has clean edges due to the aperture directly in front of it, which gives highly accurate values for the beam size when using the provided FWHM. However, if the beam has a less rectangular shape, the determination of the beam size is less accurate. The size of all screens (screen1 to screen4) is identical, in order to facilitate comparability.
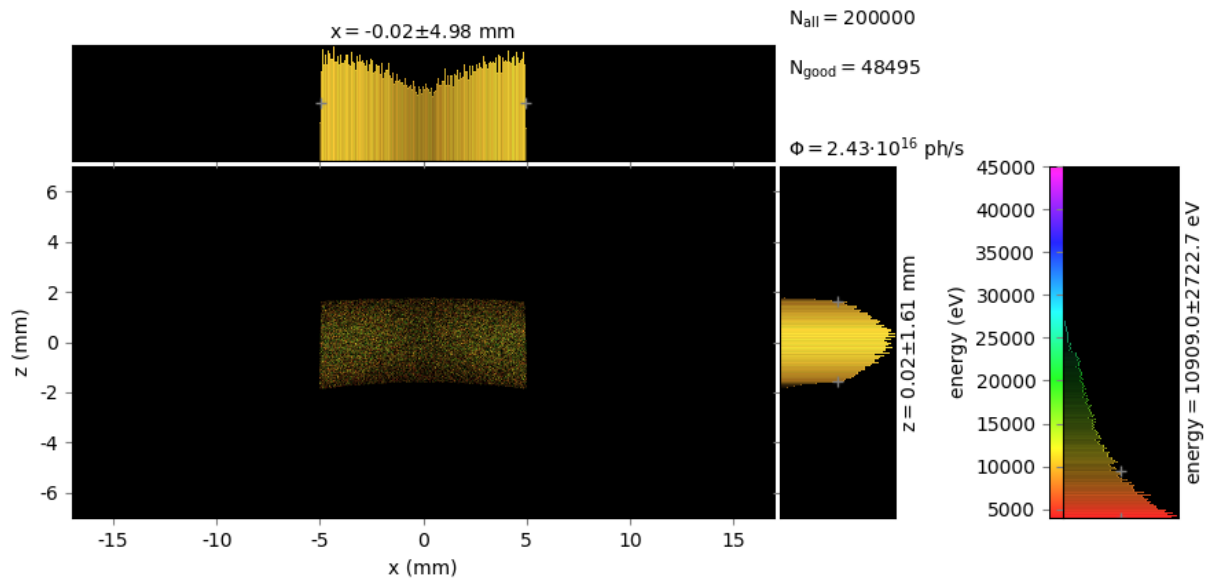

Figure 22: Example graphic resulting from xrt calculations for a the use of a toroidal mirror at II position with length 1400 mm and incidence angle 2.5 mrad at screen3. The thee 1D histograms describe the energy distribution as well as the flux distribution in x and z direction, respectively. In addition, the center and FWHM of these 1D histograms are presented. The central 2D histogram is displaying the beam shape (x and z axis of the screen).

A.3. Details on Calculations

The calculations up to screen3 (last screen before DCM, see Fig. 7) cover the entire energy range of the AppAnaXAFS beamline from 4 keV to 45 keV. The calculations for screen4 after the DCM were performed separately as the energy selection naturally reduces the flux significantly, which in turn requires a higher number of created rays and, thus, higher calculation time. However, most of the rays generated for the previous screens are not relevant for the calculations on screen4, as the DCM only allows those with acceptable energy to pass. Therefore, we reduced the energy range to ± 5 eV or ± 15 eV around the chosen base energy of 9 keV or 22 keV, respectively.

References

[1] DECHEMA e. V. Homepage of NFDI (Nationale Forschungsdateninfrastruktur) for Catalysis related Science. https://nfdi4cat.org, 6 2022.

[2] D. Doronkin. Private communication on catalytitc experiments during beamtimes at P64 and P65, 2023.

[3] M. Wu, G. Zhang, H. Tong, X. Liu, L. Du, N. Chen, J. Wang, T. Sun, T. Regier, and Sun. S. Cobalt (II) oxide nanosheets with rich oxygen vacancies as highly efficient bifunctional catalysts for ultra-stable rechargeable Zn-air flow battery. *Nano Energy*, 79:105409, 2021. 10.1016/j.nanoen.2020.105409.

[4] E. Marini, D. O. De Souza, G. Aquilanti, M. Liebert, F. Rossi, and B. Bozzini. Operando XAS of a Bifunctional Gas Diffusion Electrode for Zn-Air Batteries under Realistic Application Conditions. *Applied Sciences*, 11:11672, 2021. 10.3390/app112411672.

[5] J. Kim, S.-J. Kim, E. Jung, D. H. Mok, V. K. Paidi, J. Lee, H. S. Lee, Y. Jeoun, W. Ko, H. Shin, B.-H. Lee, S.-Y. Kim, H. Kim, J. H. Kim, S.-P. Cho, K.-S. Lee, S. Back, S.-H. Yu, Y.-E. Sung, and T. Hyeon. Atomic Structure Modification of Fe – N – C Catalysts via Morphology Engineering of Graphene for Enhanced Conversion Kinetics of Lithium-Sulfur Batteries. *Advanced Functional Materials*, 32:2110857, 2022. 10.1002/adfm.202110857.

[6] A. Chapovetsky, R. M. Kennedy, R. Witzke, E. C. Wegener, F. Dogan, P. Patel, M. Ferrandon, J. Niklas, O. G. Poluektov, N. Rui, S. D. Senanayake, J. A. Rodriguez, N. J. Zaluzec, L. Yu, J. Wen, C. Johnson, C. J. Jenks, A. J. Kropf, C. Liu, M. Delferro, and D. M. Kaphan. Lithium-Ion Battery Materials as Tunable, "Redox Non-Innocent" Catalyst Supports. *ACS Catalysis*, 12:7233, 2022. 10.1021/acscatal.2c00935.

[7] B. Yang, H. Li, Z. Zhang, K. Xiao, M. Yang, F. Zhang, M. Wang, X. Guo, Q. Li, W. Fu, R. Si, L. Wang, and H. Chen. Nickel dual-atom catalysts for the selective electrocatalytic debromination of tribromoacetic acid as a green chemistry process. *Chemical Engineering Journal*, 427:131719, 2022. 10.1016/j.cej.2021.131719.

[8] M. Guo, M. J. Gray, H. Job, C. Alvarez-Vasco, S. Subramaniam, X. Zhang, L. Kovarik, V. Murugesan, S. Phillips, and K. K. Ramasamy. Uncovering the active sites and demonstrating stable catalyst for the cost-effective conversion of ethanol to 1-butanol. *Green Chemistry*, 23:8030, 2021. 10.1039/D1GC01979A.

[9] Y. Injongkol, P. Khemthong, N. Yodsin, Y. Wongnongwa, N. Sosa, S. Youngjan, T. Butburee, B. Rungtaweevoranit, S. Kiatphuengporn, J. Wittayakun, F. Roessner, and S. Jungsuttiwong. Combined in situ XAS and DFT studies on the role of Pt in zeolite-supported metal catalysts for selective n-hexane isomerization. *Fuel*, 314:123099, 2022. 10.1016/j.fuel.2021.123099.

[10] L. J. A. Macedo, A. A. E. Santo, G. C. Sedenho, A. Hassan, R. M. Iost, G. T. Feliciano, and F. N. Crespilho. Three-dimensional catalysis and the efficient bioelectrocatalysis beyond surface chemistry. *Journal of Catalysis*, 401:200, 2021. 10.1016/j.jcat.2021.07.022.

[11] N. Kochaputi, P. Khemthong, P. Kasamechonchung, T. Butburee, W. Limphirat, Y. Poo-arporn, S. Kuboon, K. Faungnawakij, and C. Kongmark. Roles of supports on reducibility and activities of Cu_3P catalysts for deoxygenation of oleic acid: In situ XRD and XAS studies. *Molecular Catalysis*, 523:111425, 2022. 10.1016/j.mcat.2021.111425.

[12] M. Chen, D. A: Cullen, S. Karakalos, X. Lu, J. Cui, A. J. Kropf, H. Mistry, K. He, D. J. Myers, and G. Wu. Single Atomic Iron Site Catalysts via Benign Aqueous Synthesis for Durability Improvement in Proton Exchange Membrane Fuel Cells. *Journal of the Electrochemical Society*, 168:044501, 2021. 10.1149/1945-7111/abf014.

[13] J. Kang, Q.-Y. Fan, W. Zhou, Q. Zhang, S. He, L. Yue, Y. Tang, L. Nguyen, X. Yu, Y. You, H. Chang, X. Liu, L. Chen, Y. Liu, F. Tao, J. CHeng, and Y. Wang. Iridium boosts the selectivity and stability of cobalt catalysts for syngas to liquid fuels. *Chem*, 8:1050, 2022. 10.1016/j.chempr.2021.12.016.

[14] E. Valle, M. S. Duyar, J. L. Snider, S. K. Regli, M. Rønning, A. Gallo, and T. F. Jaramillo. In Situ Studies of the Formation of MoP Catalysts and Their Structure under Reaction Conditions for Higher Alcohol Synthesis: The Role of Promoters and Mesoporous Supports. *The Journal of Physical Chemistry C*, 126:5575, 2022. 10.1021/acs.jpcc.2c00837.

[15] A. C. Thompson, D. Lindau, I. Attwood, Y. Liu, E. Gullikson, P. Pianetta, M. Howells, A. Robinson, K.-J. Kim, J. Scofield, J. Kirz, J. Underwood, J. Kortright, G. Williams, and H. Winick. *X-Ray Data Booklet*. Lawrence Berkeley National Laboratory, 2009.

[16] Go FAIR. Homepage of Go FAIR. https://www.go-fair.org/, 1 2022.

[17] Deutsches Elektronen-Synchrotron DESY. ROCK IT webpage. https://www.rock-it-project.de/, 2023.

[18] K. Kiefer, L. Rossa, F. Wutzler, N. Ektröm, A. Pettersson, E. Faulhaber, and M. Zolliker. An introduction to SECoP – the sample environment communication protocol . *Journal of Neutron Research*, 21:181, 2019. 10.3233/JNR-190143.

[19] Heinz Maier-Leibnitz Zentrum. Homepage of NICOS – Network Instrument COntrol System. https://nicos-controls.org/, 2023.

[20] DAPHNE4NFDI. DAPHNE4NFDI Homepage (Data for Photon and Neutron Experiments for Nationale Forschungsdateninfrastruktur). https://www.daphne4nfdi.de/english/index.php, 9 2022.

[21] DAPHNE4NFDI. DAPHNE4NFDI work meeting 2022. https://events.hifis.net/event/569/, 12 2022. 5 – 7 December 2022, Hamburg.

[22] Deutsches Elektronen-Synchrotron DESY. DESY Photon Science Users' Meeting – Overview Satellite Meetings. https://indico.desy.de/event/36974/page/4290-overview-satellite-meetings, 01 2023.

[23] Helmholtz-Zentrum Berlin. Hands on Workshop for SECoP. https://www.helmholtz-berlin.de/events/secop/index_en.html, 2023. 22 – 23 February 2023, Berlin.

[24] Argonne National Laboratory. Advanced Photon Source Upgrade Project Final Design Report, 2019. Chapter 4: Experimental Facilities, https://www.aps.anl.gov/sites/www.aps.anl.gov/files/APS-Uploads/Aps-Upgrade/FDR/Chapter%204%20-%20Experimental%20Facilities.pdf.

[25] K. Klementiev, K. Norén, S. Carlson, K. G. V Sigfridsson Clauss, and I. Persson. The BALDER Beamline at the MAX IV Laboratory. *Journal of Physics: Conference Series*, 712:012023, 2016. 10.1088/1742-6596/712/1/012023.

[26] Balder, 2021. https://www.maxiv.lu.se/accelerators-beamlines/beamlines/balder/.

[27] S. Pascarelli, O. Mathon, T. Mairs, I. Kantor, G. Agostini, C. Strohm, S. Pasternak, F. Perrin, G. Berruyer, P. Chappelet, Clavel C., and M. C. Dominguez. The Time-resolved and Extreme-conditions XAS (TEXAS) facility at the European Synchrotro nRadiation Facility: the energy-dispersive X-ray absorption spectroscopy beamline ID24. *Journal of Synchrotron Radiation*, 23:353, 2015. 10.1107/S160057751501783X.

[28] ID26 – X-ray absorption and emission spectroscopy, 2021. https://www.esrf.eu/UsersAndScience/Experiments/EMD/ID26.

[29] Beamline Details of ID26, ESRF-EBS, 2021. private communication with Pieter Glatzel.

[30] Brazilian Synchrotron Light Laboratory. EMA Beamline, 2020. https://www.lnls.cnpem.br/facilities/ema-en/.

[31] R. D. dos Reis, U. F. Kaneko, B. A. Francisco, J. Fonseca Jr., M. A. S. Eleoterio, and N. M. Souza-Neto. Preliminary Overview of the Extreme Condition Beamline (EMA) at the new Brazilian Synchrotron Source (Sirius). *Journal of Physics: Conference Series*, 1609, 2020. 10.1088/1742-6596/1609/1/012015.

[32] Brazilian Synchrotron Light Laboratory. QUATI Beamline, 2021. https://www.lnls.cnpem.br/facilities/quati-en/.

[33] DESY Photon Science. P62 SAXSMAT, 2023. https://photon-science.desy.de/facilities/petra_iii/beamlines/p64_advanced_xafs/index_eng.html.

[34] DESY Photon Science. P64 Advanced X-ray Absorption Spectroscopy, 2021. https://photon-science.desy.de/facilities/petra_iii/beamlines/p64_advanced_xafs/index_eng.html.

[35] W. A. Caliebe, V. Murzin, A. Kalinko, and M. Görlitz. High-flux XAFS-beamline P64 at PETRA III. *AIP Conference Proceedings*, 2054, 2019. 10.1063/1.5084662.

[36] DESY Photon Science. P65 Applied X-ray Absorption Spectroscopy, 2021. https://photon-science.desy.de/facilities/petra_iii/beamlines/p65_applied_xafs/index_eng.html.

[37] Deutsches Elektronen-Synchrotron DESY. PETRA IV, New Dimensions – Partner for research and industry. https://petra4.desy.de/petra_iv/users_and_industry/index_eng.html, 11 2022.

[38] K. Klementiev and R. Chernikov. Powerful scriptable ray tracing package xrt. In *Advances in Computational Methods for X-Ray Optics III*, volume 9209, page 92090A. International Society for Optics and Photonics, 2014. 10.1117/12.2061400.

[39] M. Nentwich, O. Seeck, M. Krisch, and E. Welter. X-ray tracing study of different mirror placements for a potential 3-pole Wiggler use at future AppAnaXAS beamline. https://bib-pubdb1.desy.de/record/601181, 1 2024.

[40] K. Bagschik. Confluence webpage of the Applied Analytical XAFS and Q-EXAFS Beamline. https://confluence.desy.de/display/WRT/Applied+Analytical+XAFS+and+Q-EXAFS+Beamline, 10 2022.

[41] I. V. Agapov, S. A. Antipov, R. Bartolini, R. Brinkmann, Y.-C. Chae, D. Einfeld, T. Hellert, M. Hüning, M. A. Jebramcik, J. Keil, C. Li, and R. Wanzenberg. PETRA IV Storage Ring Design. In *Proceedings of the 13th International Particle Accelerator Conference (IPAC'22)*. JACoW Publishing, Geneva, Switzerland, 07 2022. 10.18429/JACoW-IPAC2022-TUPOMS014.

[42] H. Schulte-Schrepping. Private communication on the equipment in the tunnels. 09.05.2023 and 07.08.2023.

[43] D. Raoux. *Neutron and Synchrotron Radiation for Condensed Matter Studies*, volume I – Theory, Instrumentation and Methods, chapter II – Introduction to Synchrotron Radiation and to the Physics of Storage Rings, page 37. EDP Sciences – Springer-Verlag, 1993.

[44] E. Welter. Private communication on spectroscopic experiments at P65, 2023.

[45] E. Welter, U. Bösenberg, R. Chernikov, G. Falkenberg, and G. Wellenreuther. EXAFS with synchronised undulator gap – monochromator scans at PETRA III beamline P06, 2012. https://photon-science.desy.de/annual_report/files/2012/20122142.pdf.

[46] E. A. Schneidmiller and M. V. Yurkov. Undulator Tapering. https://www.desy.de/xfel-beam/data/talks/files/2016.01.02_12_13_13_21_1_20151201_FELSeminar_Yurkov_Tapering.pdf, 2015. FEL Seminar, 1 December 2015, European XFEL, Hamburg.

[47] S. C. Gottschalk, D. C. Quimby, and W. D. Kimura. Gap-tapered undulators for high-photonenergy synchrotron radiation production. *AIP Conference Proceedings*, 521, 2000. 10.1063/1.129181.

[48] B. Bornmann, J. Kläs, O. Müller, D. Lützenkirchen-Hecht, and R. Frahm. The quick EXAFS setup at beamline P64 at PETRA III for up to 200 spectra per second. *AIP Conference Proceedings*, 2054, 2019. 10.1063/1.5084609.

[49] H. Winick, G. Brown, K. Halbach, and J. Harris. Wiggler and Undulator Magnets. *Physics Today*, 34:50, 1981.

[50] S. M. Liuzzo, N. Carmignani, J. Chavanne, L. Farvacque, B. Nash, and P. Raimondi. Optics adaptions for bending magnet beamlines at ESRF: Short bend, 2-pole Wiggler, 3-pole Wiggler. *Proceedings of IPAC2017 (International Particle Accelerator Conference)*, page 666, 2017. https://accelconf.web.cern.ch/IPAC2017/papers/mopik062.pdf, 05 Beam Dynamics and Electromagnetic Fields, D01 Beam Optics – Lattices, Correction Schemes, Transport.

[51] G. Brown, K. Halbach, J. Harris, and H. Winick. Wiggler and undulator magnets – A Review. *Nuclear Instruments and Methods*, 208, 1983. 10.1016/0167-5087(83)91105-5.

[52] R. Khubbutdinov. Private communication on the properties of a 3-pole Wiggler, 2023.

[53] H. Tanaka, T. Ishikawa, S. Goto, S. Takano, T. Watanabe, and M. Yabashi. Spring-8 upgrade project. *Journal of Synchrotron Radiation*, 28:1267, 2021. .

[54] A. T. Macrander and X. R. Huang. Synchrotron X-Ray Optics. *Annual Review of Materials Research*, 47:135, 2017. 10.1146/annurev-matsci-070616-124228.

[55] F. Hippert, E. Giessler, J. L. Hodeau, E. Lelièvre-Berna, and J. R. Regnard. *Neutron and X-ray Spectroscopy*. Springer, 2006.

[56] M. Knapp and I. Pera. ROBL Upgrade Workshop: The Materials Science and Powder Diffraction Beamline MSPD at ALBA. https://www.hzdr.de/db/Cms?pOid=28050, 02 2009.

[57] J. W. M. DuMond. Theory of the use of more than two successive x-ray crystal reflections to obtain increased resolving power. *Physical Review*, 52, 1937. 10.1103/PhysRev.52.872.

[58] W. J. Bartels. Characterization of thin layers on perfect crystals with a multipurpose high resolution x-ray diffractometer. *Journal of Vacuum Science and Technology B*, 1, 1983. 10.1116/1.582553.

[59] D. Lübbert, A. Meents, and E. Weckert. Accurate rocking-curve measurements on protein crystals grown in a homogeneous magnetic field of 2.4 T. *Acta Crystallographica D*, 60:987, 2004. 10.1107/S0907444904005268.

[60] U. Bonse and M. Hart. Tailless X-ray single-crystal reflection curves obtained by multiple reflection. *Applied Physics Letters*, 7, 1965. 10.1063/1.1754396.

[61] A. H. Clark, J. Imbao, R. Frahm, and M. Nachtegaal. ProQEXAFS: a highly optimized parallelized rapid processing software for QEXAFS data. *Journal of Synchrotron Radiation*, 27:551, 2019. 10.1107/S1600577519017053.

[62] J. A. Van Bokhoven and C. Lamberti. *X-ray absorption and X-ray emission spectroscopy: theory and applications*, volume 1, chapter 7 – QEXAFS: techniques and scientific applications for time-resolved XAS, page 155. John Wiley & Sons, 2016. QEXAFS: Techniques and Scientific Applications for Time-Resolved XAS by Nachtegaal, M. and Müller, O. and König, C. and Frahm, R.

[63] V. Briois, C. La Fontaine, S. Belin, L. Barthe, T. Moreno, V. Pinty, A. Carcy, R. Girardot, and E. Fonda. ROCK: the new Quick-EXAFS beamline at SOLEIL. *Journal of Physics: Conference Series*, 712, 2016. 10.1088/1742-6596/712/1/012149.

[64] T. Salditt and M. Osterhoff. *Topics in Applied pHysics*, volume 134 – Nanoscale Photonic Imaging, chapter Cahpter 3: X-ray Focusing and Optics, page 71. SpringerOpen, 2021. 10.1007/978-3-030-34413-9.

[65] P. Sainctavit, J. Petiau, A. Maceau, R. Rivallant, M. Belakhovsky, and G. Renaud. A two mirror device for harmonic rejection. *Nuclear Instruments and Methods in Physics Research A*, 273, 1988. 10.1016/0168-9002(88)90845-5.

[66] A. Freund. *X-Ray Optics for Synchrotron Radiation*, volume 1, chapter III, page 79. EDP Sciences – Springer-Verlag, 1993.

[67] E. Hecht. *Optics*. Addison Wesley, 4th edition, 2002.

[68] Thorlabs. Insights – Spherical vs. Parabolic Mirror Focal Regions. https://www.thorlabs.com/newgrouppage9.cfm?objectgroup_id=14211, 12 2019.

[69] P. Kirkpatrick and A. V. Baez. Formation of optical images by X-rays. *Journal of the Optical Society of America*, 38:766, 1948.

[70] V. V. Lider. Kirkpatrick–Baez and Wolter X-Ray Focusing Optics (Review). *Journal of Surface Investigation: X-ray, Synchrotron and Neutron Techniques*, 13:670, 2019. 10.1134/S102745101904027X.

[71] Z. Yin, H. Löchel, J. Rehanek, C. Goy, A. Kalinin, A. Schottelius, F. Trinter, P. Miedema, A. Jain, J. Valerio, P. Busse, F. Lehmkühler, J. Möller, G. Grübel, A. Madsen, J. Viefhaus, R. E. Grisenti, M. Beye, A. Erko, and S. Techert. X-ray spectroscopy with variable line spacing based on reflection zone plate optics . *Optics Letters*, 43:4390, 2018. 10.1364/OL.43.004390.

[72] A. V. Baez. Fresnel Zone Plate for optical image formation using extreme ultraviolet and soft x radiation. *Journal of the Optical Society of America*, 51:405, 1961. 10.1364/JOSA.51.000405.

[73] A. Snigirev, V. Kohn, I. Snigirev, and B. Lengeler. A compound refractive lens for focusing high-energy X-rays. *Nature*, 384:49, 1996. 10.1038/384049a.

[74] A. Snigirev, I. Snigireva, G. Vaughan, J. Wright, M. Rossat, A. Bythckov, and C. Curfs. High energy X-ray transfocator based on Al parabolic refractive lenses for focusing and collimation. *Journal of Physics: Conference Series*, 186:012073, 2009. 10.1088/1742-6596/186/1/012073.

[75] K. Schwarzschild. Untersuchungen zur geometrischen Optik. *II. Astronomische Mitteilungen der Königlichen Sternwarte zu Göttingen*, 10:4, 1905.

[76] K. Reinsch and A. D. Wittmann. *Karl Schwarzschild – Wegbereiter moderner Teleskopoptik*. Universitätsverlag, Göttingen, 2017.

[77] H. Wolter. Spiegelsysteme streifenden Einfalls als abbildende Optiken für Röntgenstrahlen. *Annalen der Physik*, 10:94, 1952. 10.1002/andp.19524450108.

[78] M. Montel. X-ray microscopy with catamegonic roof mirrors. *X-ray Microscopy and Microradiography*, page 177, 1957.

[79] G. B. M. Vaughan, J. P. Wright, A. Bytchkov, M. Rossat, H. Gleyzolle, I. Snigireva, and A. Snigirev. X-ray transfocators: focusing devices based on compound refractive lenses. *Journal of Synchrotron Radiation*, 18:125, 2019. 10.1107/S0909049510044365.

[80] C. Braig, H. Löchel, A. Firsov, M. Brzhezinskazya, A. Hafner, J. Rehanek, M. Wojcik, A. Marcrander, L. Assoufid, and A. Erko. Hard x-ray spectroscopy and imaging by a reflection zone plate in the presence of astigmatism. *Optics Letters*, 41, 2016. .

[81] NTT Advanced Technology Corporation. X-ray Fresnel zone plate. webpage, 2023. https://keytech.ntt-at.co.jp/en/xray/prd_0002.html.

[82] rxoptics. Refractive X-ray Optics – Design parameters, 2023. https://www.rxoptics.de/design-parameters/.

[83] NOB Nano Optics Berlin GmbH. Nano Optics Berlin, webpage. https://www.nanooptics-berlin.com/, 2023.

[84] E. Welter. Short manual for beamline P65. Handout at beamline, 2023.

[85] J. Morse. *Neutron and Synchrotron Radiation for Condensed Matter Studies*, volume I – Theory, Instrumentation and Methods, chapter IV – Detectors for Synchrotron Radiation, page 95. EDP Sciences – Springer-Verlag, 1993.

[86] F. W. Lytle, R. B. Greegor, D. R. Sandstorm, E. C. Marques, J. Wong, C. L. Spiro, G. P. Huffman, and F. E. Huggins. Measurement of soft X-ray absorption spectra with a fluorescent ion chamber detector. *Nuclear Instruments and Methods in Physics Research*, 226:542, 1984. 10.1016/0168-9002(84)90077-9.

[87] P. Lechner, C. Fiorini, R. Hartmann, J. Kemmer, N. Krause, P. Leutenegger, A. Longoni, H. Soltau, D. Stötter, R. Stötter, L. Strüder, and U. Weber. Silicon drift detectors for high count rate X-ray spectroscopy at room temperature. *Nuclear Instruments and Methods in Physics Research A*, 458:281, 2001. 10.1016/S0168-9002(00)00872-X.

[88] L. Strüder, P. Lechner, and P. Leutenegger. Silicon drift detector – the key to new experiments. *Science of Nature*, 85, 1998. 10.1007/s001140050545.

[89] W. Caliebe. Private communication on spectroscopic experiments at P64, 2023.

[90] Dectris. EIGER2 for Synchrotrons. https://www.dectris.com/detectors/x-ray-detectors/eiger2/eiger2-for-synchrotrons/, 2023.

[91] X-Spectrum. Lambda X-Ray Detector, 2023. https://x-spectrum.de/products/lambda/.

[92] O. Bunemann, T. E. Cranshaw, and J. A. Harvey. Design of Grid Ionization Chambers. *Canadian Journal of Research*, 27a, 1949. 10.1139/cjr49a-019.

[93] A. Al-Adili, F. Hambsch, R. Bencardino, S. Pomp, S. Oberstedt, and S. Zeynalov. On the Frisch–Grid signal in ionization chambers. *Nuclear Instruments and Methods in Physics Research A*, 671:103, 2012. 10.1016/j.nima.2011.12.047.

[94] KIT AK Grunwaldt. Homepage of Arbeitskreis Grunwaldt, 11 2023. https://www.itcp.kit.edu/grunwaldt/index.php.

[95] M. Schroer, A. Levish, Y. Yildizlar, M. Stepponat, and M. Winterer. A versatile chemical vapor synthesis reactor for *in situ* x-ray scattering and spectroscopy. *Review of Scientific Instruments*, 93:113706, 2022. 10.1063/5.0122461.

[96] D. Eggart, A. Zimina, G. Cavusoglu, M. Casapu, D. E. Doronkin, K. A. Lomachenko, and J.-D. Grunwaldt. Versatile and high temperature spectroscopic cell for operando fluorescence and transmission x-ray absorption spectroscopic studies of heterogeneous catalysts. *Review of Scientific Instruments*, 92:023106, 2021. 10.1063/5.0038428.

[97] P. Jäker, D. Aegerter, T. Kyburz, R. Städler, R. Fonjallaz, B. Detlefs, and D. Koziej. Flow cell for operando X-ray photon-in-photon-out studies on photo-electrochemical thin film devices. *Open Research Europe*, 2:74, 2023. 10.12688/openreseurope.14433.2.

[98] F. Eckelt, P. Rothweiler, F. Braun, L. Voss, A. Šarić, M. Vrankić, and D. Lützenkirchen-Hecht. In Situ Observation of ZnO Nanoparticle Formation by a Combination of Time-Resolved X-ray Absorption Spectroscopy and X-ray Diffraction. *materials*, 15, 2022. 10.3390/ma15228186.

[99] Sardana Home Page. https://www.sardana-controls.org/, 1 2023.

[100] ESRF. BLISS documentation, 02 2023. https://bliss.gitlab-pages.esrf.fr/bliss/master/, https://slides.com/matiasg/bliss_bessy/fullscreen#/1.

[101] D. Allan, T. Caswell, S. Campbell, and M. Rakitin. Bluesky's Ahead: A Multi-Facility Collaboration for an a la Carte Software Project for Data Acquisition and Management. *Synchrotron Radiation News*, 32(3):19, 2019. 10.1080/08940886.2019.1608121.

[102] bluesky. Bluesky project homepage, 02 2023. https://blueskyproject.io/.

[103] Brookhaven National Lab. Homepage of ophyd. https://nsls-ii.github.io/ophyd/, 11 2023.

[104] DESY HASYLAB. Tango at Hasylab. http://hasyweb.desy.de/services/computing/Tango/node3.html, 2 2023.

[105] ISSE. Sample Environment Communication Protocol. https://sampleenvironment.org/committees/secop/, 2 2023.

[106] ESS. ESS EPICS Environment (e3). http://e3.pages.esss.lu.se/, 2 2023.

[107] B. Hinrichsen. Relevanz von Automatisierung in der Industrie. Talk at the DESY Photon Science Users' Meeting, 2023. January 2023, Hamburg, Germany.

[108] Karlsruhe Nano Micro Facility (KNMF). KNMF Laboratory for Micro- and Nanostructuring – Surface-Anchored Metal-Organic Frameworks (SURMOFs. https://www.knmf.kit.edu/downloads/KNMF_Technology_Description_1_IFG_SURMOFs.pdf, 2023.

[109] Deutsches Elektronen-Synchrotron DESY. Homepage of DOOR – DESY Online Office for Research with Photons, 12 2023. https://door.desy.de/door/.

[110] Deutsches Elektronen-Synchrotron DESY. Homepage of gamma-portal – Data Management for Photon-Science, 12 2023. https://gamma-portal.desy.de/pls/apex/f?p=260:LOGIN::::::.

[111] J. Hodson, S. Collins, F. Genova, N. Harrower, S. Jones, L. Laaksonen, D. Mietchen, R. Petrauskaité, and P. Wittenburg. Turning FAIR data into reality. Interim Report from the European Commission Expert Group on FAIR data, 6 2018. 10.5281/zenodo.1285272.

[112] The HDF group. webpage of the hdf5 library and file format, 11 2023. https://www.hdfgroup.org/solutions/hdf5/.

[113] A. Rothkirch. Confluence page of Data Storage Guidelines at DESY-FS, 08 2023. https://confluence.desy.de/display/FSEC/Data+Storage+Guidelines+at+DESY-FS.

[114] B. Ravel. ATHENA: XAS Data Processing, 03 2023. https://bruceravel.github.io/demeter/documents/Athena/index.html.

[115] The International X ray Absorption Society (IXAS). Webpage of the XDI Data Format, 12 2023. https://docs.xrayabsorption.org/xaslib/xdi.html.

[116] NeXus International Advisory Committee. webpage About the NeXus Data Format, 11 2023. .

[117] Go FAIR. Homepage of The ICAT Project. https://icatproject.org/, 11 2023.

[118] SciCat. webpage of SciCat – Manage and annotate your scientific data, 11 2023. https://scicatproject.github.io/, https://www.psi.ch/de/awi/scicat.

[119] PGI / JCNS Scientific IT-Systems. Homepage of SampleDB. https://scientific-it-systems.iffgit.fz-juelich.de/SampleDB/, 11 2023.

[120] Google. Homepage of GoogleDocs, 11 2023. https://www.google.de/intl/de/docs/about/.

[121] Nicolas CARPi. Homepage of eLabFTW, 11 2023. https://www.elabftw.net/.

[122] SciNote LLC. Homepage of SciNote – Electronic Lab Notebook & Lab Inventory Management Software, 11 2023. https://www.scinote.net/.

[123] ETH Zürich. Webpage of openBIS, 11 2023. https://scicatproject.github.io/, https://www.psi.ch/de/awi/scicat.

[124] CERF. Webpage of CERF, 11 2023. https://cerf-notebook.com/.

[125] KIT. Webpage of Chemotion, 11 2023. https://chemotion.net/.

[126] M. Scheidgen, L. Himanen, A. Ladines, A. Sikter, M. Nakhaee, A. Fekete, T. Chang, A. Golparvar, J. Márquez, S. Brockhauser, S. Brückner, L. Ghiringhelli, F. Dietrich, D. Lehmberg, T. Denell, A. Albino, H. Näsström, S. Shabih, F. Dobener, M. Kühbach, R. Mozumder, J. Rudzinski, N. Daelman, J. Pizarro, M. Kuban, P. Salazar, C. ad Ondračka, H.-J. Bungartz, and C. Draxl. NOMAD: A distributed web-based platform for managing materials science research data. *Journal of Open Source Software*, 8:5388, 2023. https://doi.org/10.21105/joss.05388.

[127] Colabra Inc. Homepage of Colabra, 11 2023. https://www.colabra.ai/.

[128] LabTwin GmbH. Homepage of Labfolder. https://www.labtwin.com/, 11 2023.

[129] Labforward GmbH. Homepage of LabTwin. https://labfolder.com/imprint/, 11 2023.

[130] The International X ray Absorption Society (IXAS). X-ray Absorption Data Library, 11 2023. https://xaslib.xrayabsorption.org/elem/.

[131] Canadian Light Source. X-ray Absorption Spectroscopy (XAS) Database, 11 2023. https://xasdb.lightsource.ca/.

[132] Helmholtz-Zentrum Dresden-Rossendorf (HZDR). Actinide reference database for Spectroscopy (formerly AcXAS), 11 2023. https://www.hzdr.de/db/acxas.www.welcome.

[133] Berkeley lab. The Materials Project – X-ray Absorption Spectra, 11 2023. https://next-gen.materialsproject.org/xas.

[134] A. Gaur, S. Paripsa, F. Förste, D. Doronkin, W. Malzer, C. Schlesiger, J.-D. Grunwaldt, B. Kanngießer, D. Luetzenkirchen-Hecht, and E. Welter. XAS reference database under DAPHNE4NFDI, 2023. Poster during the DAPHNE4NFDI Annual Meeting 2023, .

[135] DESY. Homepage of ASAP::O. https://asapo.pages.desy.de/asapo/, 12 2023.